Acoustic receptivity and transition modeling of Tollmien-Schlichting disturbances induced by distributed surface roughness

Henrique Raposo,[1, 2, a)] Shahid Mughal,[1] and Richard Ashworth[2]
[1)] *Department of Mathematics, Imperial College London, South Kensington Campus, London SW7 2AZ, United Kingdom.*
[2)] *Airbus Group, Bristol BS99 7AR, United Kingdom.*

(Accepted for publication in Physics of Fluids: April 8, 2018)

Acoustic receptivity to Tollmien-Schlichting waves in the presence of surface roughness is investigated for a flat plate boundary layer using the time-harmonic incompressible linearized Navier-Stokes equations. It is shown to be an accurate and efficient means of predicting receptivity amplitudes, and therefore to be more suitable for parametric investigations than other approaches with DNS-like accuracy. Comparison with literature provides strong evidence of the correctness of the approach, including the ability to quantify non-parallel flow effects. These effects are found to be small for the efficiency function over a wide range of frequencies and local Reynolds numbers. In the presence of a two-dimensional wavy-wall, non-parallel flow effects are quite significant, producing both wavenumber detuning and an increase in maximum amplitude. However, a smaller influence is observed when considering an oblique Tollmien-Schlichting wave. This is explained by considering the non-parallel effects on receptivity and on linear growth which may, under certain conditions, cancel each other out. Ultimately, we undertake a Monte-Carlo type uncertainty quantification analysis with two-dimensional distributed random roughness. Its power spectral density (PSD) is assumed to follow a power law with an associated uncertainty following a probabilistic Gaussian distribution. The effects of the acoustic frequency over the mean amplitude of the generated two-dimensional Tollmien-Schlichting waves are studied. A strong dependence on the mean PSD shape is observed and discussed according to the basic resonance mechanisms leading to receptivity. The growth of Tollmien-Schlichting waves is predicted with non-linear parabolized stability equations computations to assess the effects of stochasticity in transition location.

Keywords: Acoustic receptivity, Harmonic Linear Navier Stokes, Surface roughness, Tollmien-Schlichting instability, Uncertainty quantification

I. INTRODUCTION

A laminar boundary layer lowers skin friction drag when compared to a turbulent boundary layer convecting over a surface. Prediction of the laminar to turbulent transition for a laminar boundary layer over a swept wing is therefore a central concern in the design of low drag commercial aircraft. Actively seeking to delay this phenomena in order to maximize the extent of the laminar regime and minimize drag requires a clear understanding of how transition location is affected by the external environment, wing geometry and surface finish.

In a small perturbation environment, the process leading to transition of the boundary layer can be decomposed into three stages: (i) receptivity, which entails the generation of instabilities, (ii) linear growth, and (iii) non-linear growth culminating in breakdown into the turbulent regime[1]. Non-linear growth includes saturation and the formation of secondary instabilities. For larger disturbance environments other mechanisms which bypass linear growth may come into play. This process generally involves transient growth which is described by nonmodal stability theory[2,3].

The term receptivity was coined in 1969 by Morkovin[4]. It can be defined as the means through which external disturbances penetrate the boundary layer and originate internal perturbations that play a role in boundary layer transition to turbulent flow. Early efforts to predict transition based on the linear e^N method[5,6] bypassed the receptivity stage and provided an amplification based criteria for transition prediction assuming the presence of boundary layer disturbances, most commonly as normal modes. This technique fails to account for the amplitude of the disturbances and therefore cannot be extended to correctly predict onset of the non-linear growth phase[7]. Moreover, it is a semi-empirical method because it requires calibration of the critical N-factor as a function of the flow conditions and of the disturbance environment[8]. Receptivity originated as an effort to go beyond the limitations of linear stability theory, which does not offer the degrees of freedom to incorporate the effects of the external environment in transition prediction. It is now widely accepted to be the "missing piece" that is required in order to devise a universal amplitude-based transition prediction criterion.

The external forcing of the boundary layer must satisfy the resonance condition in order to generate the normal modes described by the Orr-Sommerfeld (O-S) equation; its frequency and wavelength must match that of the eigenmode of the unstable wave. While frequency compatibility is commonly found in acoustic waves, their wavelengths are much longer. Receptivity thus occurs when this disparity in length scales is overcome through

[a)] Electronic mail: h.raposo17@imperial.ac.uk

a length-scale reduction mechanism. Goldstein[9,10] and Ruban[11] first elucidated this process by showing that receptivity occurs in non-parallel flow regions where streamwise variations of the base flow occur on the scale of the wavelength of Tollmien-Schlichting (T-S) waves. This includes the leading edge where the boundary layer is extremely thin and rapidly growing and hence presents the non-parallel flow features necessary for the length-scale reduction mechanism. The second class of non-parallel flow regions is much broader. It includes any region with a feature causing a short-scale flow perturbation of the order of the instability wavelength. Roughness elements, surface discontinuities, surface waviness, separation bubbles and suction strips constitute examples.

This paper focuses on the unswept flat plate problem and therefore on the formation of Tollmien-Schlichting waves generated by surface inhomogeneities, which are viscous instabilities. We overlook leading edge acoustic receptivity which is known to produce T-S waves with a very weak equivalent amplitude when compared to surface roughness mechanisms[9–12]. The seminal works of Ruban[11] and Goldstein[10] considered the second class of receptivity response, which gives a stronger response and is also now established to be the primary mechanism which plays a role in surface roughness induced disturbance generation. Stewartson[13,14] and Messiter's[15] triple-deck asymptotic structure was used to analytically obtain both the steady perturbation caused by the presence of a wall feature, and the T-S wave resulting from the non-linear interaction between the freestream acoustic induced Stokes layer and the steady-state perturbation. A non-linear analogue was investigated and solved numerically by Bodonyi *et al.*[16] While the high-Reynolds-number asymptotic approach reveals the physical mechanisms behind the receptivity phenomena, it is also limited for three reasons. Firstly because the triple-deck structure is only formally valid near the lower-branch of neutral stability. Secondly, it does not account for finite Reynolds number effects. Lastly, because it does not allow us to study the effects of frequency at different Reynolds numbers since these are reduced to a single parameter.

Choudhari & Streett[17,18] and Crouch[19,20] proposed a so-called finite-Reynolds-number theory (FRNT) to predict receptivity in both localized and non-localized regions, overcoming most of these limitations. Crouch & Bertolotti[21] extended the work to three-dimensional (3-D) T-S waves with so-called mode-interaction theory and a parabolized stability equations (PSE)[22] type formalism. This work was generalized for finite height humps by Nayfeh & Ashour[23], who showed agreement with the non-linear behavior for large roughness heights obtained by Saric in his acoustic receptivity experiments[24]. Wu[25] extended the asymptotic theory to distributed roughness in the presence of vortical and acoustic waves. Interestingly, when comparing the results of his second-order theory with Choudhari's[18] theory and experimental findings of Wiegel & Wlezien[26], Wu found first-order theory to be a much more consistent fit; second-order corrections gave worse agreement.

The inclusion of non-parallel effects in the finite-Reynolds number theory was done approximately by Bertolotti[27] through a Taylor expansion of the base-flow treated in Fourier space (residue-based analysis). Previous approaches[28–30] restricted their analysis to a single slowly-varying perturbation ansatz. In particular, the multiple-scales method[30] was recently applied to the linearized Navier-Stokes (LNS) equations to model receptivity[31]. The parabolized stability equations[22,32,33] also partially capture non-parallel flow effects.

Hill[34] used the properties of adjoint solutions for receptivity calculations. Even though Hill's theory is general enough to be applied to any set of equations describing boundary layer instabilities, he solved the inhomogeneous Orr-Sommerfeld equation in the presence of an acoustic wave and surface roughness. Airiau[35] and Collis & Dobrinsky[36] extended Hill's work to the parabolized stability equations in order to account for non-parallel flow effects. The adjoint parabolized stability equations had first been proposed by Herbert[22]. More recently, the same method was applied to the compressible linearized Navier-Stokes equations to model cross-flow instabilities in an infinite swept wing[37].

Due to recent advances in computational hardware and construction of efficient numerical approaches, direct numerical simulations have been gaining traction in the last 20 years[38–46]. Collis & Lele[44] studied stationary cross-flow instabilities by solving the compressible linearized Navier-Stokes equations assuming a Fourier decomposition in the spanwise direction and time-stepping the solution towards a stationary state. Lastly, De Tullio & Ruban[41] took on the acoustic receptivity problem by solving the compressible unsteady Navier-Stokes equations to compute the steady basic flows, and the LNS equations to obtain the unsteady perturbations. The vast majority of these works are computationally demanding, thus severely limiting their applicability in sensitivity and parametric investigations or design optimization analysis.

We highlight the work of Streett[46], who suggested the use of the time-harmonic linearized incompressible Navier-Stokes equations to model receptivity. Due to continued improvements in computer hardware (large memory availability, multi-core CPU's and processor speed), the harmonic LNS solution route is an appealing means to accurately and efficiently model acoustic receptivity problems. The acoustic receptivity framework considered herein extends the earlier works of Mughal & Ashworth[47] and corresponding adjoint based treatments (see Thomas, Mughal & Ashworth[37]) who used this technique in the context of modeling roughness induced stationary crossflow receptivity of a 3-D boundary-layer swept wing problem. A Monte-Carlo based uncertainty quantification (UQ) analysis was devised to provide estimates of the variances to be expected in crossflow induced transition, arising from uncertainties in the ran-

domly prescribed surface roughness description (see §VI). The core numerics and the UQ analysis used are similar to that pursued by Mughal & Ashworth[47]; though the acoustic receptivity advancement of the concept has additional challenges.

The essentials of the receptivity modelling we undertake are based on Choudhari & Streett's[17] double-parameter expansion of the exact unsteady Navier-Stokes equations into a number of sub-problems which can be solved sequentially: (i) the boundary layer base flow, (ii) the acoustic-induced Stokes shear-wave, (iii) the steady perturbation caused by the presence of surface roughness, and finally (iv) the resulting T-S disturbance. Each sub-problem is solved for in an efficient and accurate manner with a standard boundary layer solver, a linearized unsteady boundary layer equations (LUBLE) solver, a steady LNS solver, and a time-harmonic LNS solver, respectively. The last two LNS solve steps determine the total computational time to leading order. Specifically, these ultimately require the LU decomposition of a large banded matrix yielded by the discretization of the LNS equations, which is the most time-consuming aspect. To summarize, each of the Choudhari & Streett[17] FRNT stages have been replaced with more physically-correct models, which account for non-parallelism and any inherent ellipticity of the flow physics through usage of the LNS formulation.

The reasons for pursuing this methodology are threefold: it is general and versatile enough to accommodate different receptivity mechanisms (vorticity, wing vibration, suction, heating)[17], a wide range of flow conditions[41], and finally non-linear corrections (both due to finite-height roughness and interaction of acoustic modes). It is sufficiently fast to be used recurrently (one acoustic frequency scenario can currently be computed in under 5 minutes approximately, using 20 CPU cores), while also enjoying the advantage of being able to calculate receptivity amplitudes for a range of different roughness shapes at little additional computational cost.

Unlike asymptotic and finite-Reynolds number theories, important in their own right for uncovering the basic mechanisms of receptivity, the time-harmonic LNS approach is capable of fully capturing both low-Reynolds-number and non-parallel effects and thus has DNS-like accuracy. Not only is the base flow divergence taken into account, but unlike many local theories[17,19,23], the growth and evolution of the Stokes layer is also accurately modeled through the LUBLE. Apart from the boundary layer approximation used to compute the base flow and the acoustic perturbation, the validity of which has been verified many times over, one could argue that its accuracy should in every aspect be equal to that of DNS. In this paper, we show that our methodology can provide significant corrections to local theories.

The time-harmonic LNS formalism and the associated efficient LU decomposition approach yield considerable advantages in computational time over time-stepping tools when one is interested in the time-asymptotic limit behavior of a few select acoustic frequencies[46]. It is therefore more appropriate for rapid design and parametric investigations. In this paper, though we elucidate the method for the incompressible zero pressure gradient Blasius flow, we believe that with continued work the method can readily be extended to airfoil surfaces of interest in the aerospace sector.

The essential focus of the paper covers three key aspects. Firstly, we highlight the technique employed for receptivity modeling. Secondly, natural distributed surface roughness is recognized as a key feature which plays a role in the generation of T-S disturbances; the method allows this to be easily modeled. Finally, we provide a means to quantify the variance in T-S transition location that should be expected due to uncertainties arising in the surface roughness field description, which mimic the stochastic nature of real surfaces.

The remainder of this paper is structured as follows. In §II the governing equations of each term of the double-parameter expansion which allows the acoustic receptivity problem to be modeled are presented. The numerical methods employed to solve each system of equations are described in §III. The receptivity amplitude and efficiency function are defined in §IV, while §V makes a comparison between the time-harmonic LNS approach and other theoretical, numerical and experimental works, ultimately validating our approach. In §VI a Monte-Carlo type uncertainty quantification analysis with two-dimensional (2-D) randomly distributed surface roughness is undertaken. Finally, in §VII we assess the effects of the stochastic properties of distributed random roughness on transition location. Lastly, conclusions are drawn in §VIII.

II. GOVERNING EQUATIONS

Consider a flat plate and the coordinate system (x^*, y^*, z^*) positioned at its leading edge. The x^*- and z^*-axes denote the streamwise and spanwise directions respectively, whilst the y^*-axis represents the normal to the flat plate direction. The velocity components are denoted $\vec{\boldsymbol{v}}^* = [u^*, v^*, w^*]^T$. Density, dynamic viscosity, temperature and pressure are represented by ρ^*, μ^*, T^*, and p^*, respectively. Time is denoted t^*. Quantities are nondimensionalized with the velocity and density at the far-field, U_∞, ρ_∞, and the reference length scale L. The equations governing a fluid flow around a body are the Navier-Stokes (N-S) equations, to which the continuity equation is added and presented here in nondimensional incompressible form,

$$\vec{\nabla} \cdot \vec{\boldsymbol{v}} = 0 \,, \tag{1a}$$

$$\frac{\partial \vec{\boldsymbol{v}}}{\partial t} + \left(\vec{\boldsymbol{v}} \cdot \vec{\nabla}\right) \vec{\boldsymbol{v}} = -\nabla p + \frac{1}{R}\nabla^2 \vec{\boldsymbol{v}} \,, \tag{1b}$$

where $R = U_\infty L/\nu_\infty$ is the Reynolds number with the kinematic viscosity denoted by $\nu_\infty = \mu_\infty/\rho_\infty$. Dimen-

sional quantities are represented with a $*$ superscript and far-field quantities with an ∞ subscript.

A. Flow Decomposition

We now consider a plane acoustic wave traveling in the free-stream direction and the presence of a localized or distributed roughness element in the flat plate. Both the acoustic wave amplitude and the roughness element height are considered small enough such that the disturbances can be treated as small perturbations to the base flow. Consequently, a small parameter can be defined as $\varepsilon_w = h^*/L << 1$, where h^* is the maximum height or depth of the surface roughness. Similarly, $\varepsilon_a = u^*_{ac}/U_\infty << 1$ is defined, where u^*_{ac} is the maximum streamwise velocity perturbation in the freestream caused by the plane acoustic wave. A truncated double-parameter expansion is then introduced[17,48],

$$\begin{aligned}\phi(x,y,z,t) \approx &\bar{\phi}(x,y) + \varepsilon_w \hat{\phi}_w(x,y) e^{i\beta z} + \varepsilon_a \phi_a(x,y) e^{-i\omega t} \\ &+ \varepsilon_w \varepsilon_a \hat{\phi}_c(x,y) e^{i(-\omega t + \beta z)} ,\end{aligned} \tag{2}$$

where $\phi = [u, v, w, p]^T$, $\phi_w = \hat{\phi}_w(x,y)e^{i\beta z}$ and $\phi_c = \hat{\phi}_c(x,y)e^{i(-\omega t+\beta z)}$; with β representing the spanwise periodic dependence of the disturbances and surface roughness. The hat symbol generally denotes the Fourier component amplitude. The steady base flow $\bar{\phi}$ is considered strictly two-dimensional since our focus here is on the unswept flat plate problem. The steady perturbation term of order $\mathcal{O}(\varepsilon_w)$ results from the presence of either 2-D or 3-D surface roughness while the unsteady perturbation term of order $\mathcal{O}(\varepsilon_a)$ derives from the presence of a 2-D acoustic wave in the free-stream. The highest order term results from the non-linear coupling between the two previous flow perturbation terms and therefore physically represents, in general, 3-D oblique T-S waves which are the focus of this paper. Contribution from terms of higher order provide weaker corrections to the T-S wave[19] and are ignored in the present work. Fourier series decompositions are used in the spanwise direction and in time, effectively limiting the analysis to a single angular frequency and spanwise disturbance (ω, β).

The decomposition of the flow solution in these four terms is only possible because of the small perturbation assumption. The boundary conditions are transferred to the wall with a Taylor expansion, yielding

$$\begin{aligned}\vec{\boldsymbol{v}}(x,0) &= 0 , \\ \vec{\boldsymbol{v}}_w(x,0) &= -\hat{H}(x)\frac{\partial \vec{\boldsymbol{v}}}{\partial y}|_{y=0} , \\ \vec{\boldsymbol{v}}_a(x,0) &= 0 , \\ \vec{\hat{\boldsymbol{v}}}_c(x,0) &= -\hat{H}(x)\frac{\partial \vec{\boldsymbol{v}}_a}{\partial y}|_{y=0} ,\end{aligned} \tag{3}$$

where $\hat{H}(x)e^{i\beta z}$ is the Fourier component of spanwise wavenumber β of the normalized function $H(x,z)$ representing the roughness shape.

B. Unsteady Boundary Layer Equations

In the absence of surface roughness, the flow is governed to leading order by the incompressible unsteady boundary layer equations[49]:

$$\frac{\partial u^*}{\partial x^*} + \frac{\partial v^*}{\partial y^*} = 0 , \tag{4a}$$

$$\rho^*\left(\frac{\partial u^*}{\partial t^*} + u^*\frac{\partial u^*}{\partial x^*} + v^*\frac{\partial u^*}{\partial y^*}\right) = -\frac{\partial p^*}{\partial x^*} + \mu^*\frac{\partial^2 u^*}{\partial y^{*2}} , \tag{4b}$$

$$\frac{\partial p^*}{\partial y^*} = 0 . \tag{4c}$$

We introduce the change of coordinates

$$\eta = \left(\frac{U_\infty \rho_\infty}{\mu_\infty x^*}\right)^{1/2} y^* , \; x = \frac{x^*}{L} , \; t = t^*\frac{U_\infty}{L} , \tag{5}$$

and the unsteady stream function

$$\psi = \left(\frac{\mu_\infty U_\infty x^*}{\rho_\infty}\right)^{1/2} f(\eta, x, t) , \tag{6}$$

where

$$\frac{\partial \psi}{\partial y^*} = u^* = U_\infty f_\eta , \tag{7}$$

and thus to satisfy the continuity equation

$$\frac{\partial \psi}{\partial x^*} = -v^* = U_\infty\left(\frac{\mu_\infty}{x^* U_\infty \rho_\infty}\right)^{\frac{1}{2}}\left(\frac{1}{2}(f - \eta f_\eta) + x^* f_{x^*}\right) . \tag{8}$$

Using Eqs. (7) and (8) and taking into account the change of variables in Eq. (5), the unsteady x-momentum Eq. (4b) becomes

$$f_{\eta\eta\eta} + \frac{f_{\eta\eta} f}{2} = x\left(f_{\eta t} + f_\eta f_{\eta x} - f_x f_{\eta\eta} + \frac{dp}{dx}\right) , \tag{9}$$

The boundary conditions are written as,

$$f_\eta(0,x) = 0 \, , f(0,x) = 0 \, , f_\eta(\eta \to \infty, x) = 1 + \varepsilon_a e^{-i\omega t} . \tag{10}$$

The acoustic wave traveling in the free-stream manifests itself through the boundary condition as $\eta \to \infty$ and a pressure gradient. These are discussed next.

1. Acoustic Perturbation

We consider a plane acoustic wave traveling in the free-stream as a fluctuation of the unperturbed uniform steady flow,

$$\begin{aligned}\tilde{u}^*_e = U_\infty + \varepsilon_a u^*_e \, , \; \tilde{\rho}^*_e = \rho_\infty + \varepsilon_a \rho^*_e \, , \\ \tilde{p}^*_e = p_\infty + \varepsilon_a p^*_e \; , \; \tilde{T}^*_e = T_\infty + \varepsilon_a T^*_e \, ,\end{aligned} \tag{11}$$

where the acoustic fluctuations have the waveform

$$\phi_e^* = \{u_e^*, \rho_e^*, p_e^*, T_e^*\} = \hat{\phi}_e^* e^{i(-\omega^* t^* + \alpha^* x^*)} \ , \tag{12}$$

with α^* the streamwise wavenumber; the subscript e denotes the edge of the boundary layer. The freestream acoustic wave solution[50?] can be expressed as

$$\begin{aligned} \hat{u}_e^* &= U_\infty \ , \\ \hat{\rho}_e^* &= \rho_\infty M_\infty \ , \\ \hat{p}_e^* &= p_\infty \gamma M_\infty \ , \\ \hat{T}_e^* &= T_\infty \left(\gamma - 1\right) M_\infty \ , \end{aligned} \tag{13}$$

with M_∞ the far-field Mach number and γ the specific heat ratio. The streamwise wavenumber assumes the form

$$\alpha^* = \frac{\omega^* M_\infty}{U_\infty (M_\infty + 1)} \ , \tag{14}$$

if we select the downstream propagating wave. The penetration of the acoustic wave in the boundary layer is made through pressure oscillations. Special attention is required to calculate the nondimensional pressure gradient perturbation

$$\frac{\partial p_e}{\partial x} = \frac{i\omega}{(M_\infty + 1)} e^{i(-\omega t + \alpha x)} \ , \tag{15}$$

which in the incompressible limit reduces to

$$\frac{\partial p_e}{\partial x} = i\omega e^{-i\omega t} \ . \tag{16}$$

The acoustic perturbation of order $\mathcal{O}(\varepsilon_a)$ is governed by the fully elliptic linearized Navier-Stokes equations. An alternative and simpler model, though still quite accurate, is based on the LUBLE, where the unsteady pressure gradient perturbation in the wall-normal direction is neglected[9]. Similar to Prandtl's boundary-layer concept of invariance of the pressure field across the boundary-layer, coupled with the assumption of the streamwise diffusion terms being negligible, the LUBLE set can be solved by an efficient parabolic streamwise marching procedure. This is the approach utilized by us, hence an expansion of the unsteady flow variable $f(\eta, x)$ into a steady $B(\eta, x)$ and perturbed unsteady form $f_a(\eta, x)$ is thus considered,

$$f(\eta, x, t) = B(\eta, x) + \varepsilon_a f_a(\eta, x) e^{-i\omega t} \ , \tag{17}$$

which after substitution in Eq. (9) yields to leading order,

$$B_{\eta\eta\eta} + \frac{B_{\eta\eta} B}{2} = x \left(B_\eta B_{\eta x} - B_{\eta\eta} B_x + \frac{dP}{dx} \right) \ , \tag{18}$$

and to order $\mathcal{O}(\varepsilon_a)$,

$$\begin{aligned} &\frac{\partial^3 f_a}{\partial \eta^3} + \frac{B_{\eta\eta}}{2} f_a + \frac{B}{2} \frac{\partial^2 f_a}{\partial \eta^2} = \\ &x \left[i\omega \mathfrak{B} + B_\eta \frac{\partial^2 f_a}{\partial \eta \partial x} - B_{\eta\eta} \frac{\partial f_a}{\partial x} + B_{\eta x} \frac{\partial f_a}{\partial \eta} - B_x \frac{\partial^2 f_a}{\partial \eta^2} \right] \ , \end{aligned} \tag{19}$$

with

$$\mathfrak{B} = 1 - \frac{\partial f_a}{\partial \eta} \ ,$$

where the steady pressure gradient is given by dP/dx to leading order, and by Eq. (16) to order $\mathcal{O}(\varepsilon_a)$. Equation (18) reduces to the well-known Blasius equation for a zero-pressure gradient driven flow ($dP/dx = 0$), since self-similarity holds $B_{\eta x} = B_x = 0$. Upon performing these simplifications, Eq. (19) is equivalent to Eq. (2.17) of Ackerberg and Phillips' work[?] and is the equation defining the LUBLE. The unsteady boundary conditions are written as,

$$\begin{aligned} &f_a(0, x) = 0 \ , \ \frac{\partial f_a}{\partial \eta}(0, x) = 0 \\ &\frac{\partial f_a}{\partial \eta}(\eta \to \infty, x) = 1 \ , \end{aligned} \tag{20}$$

which satisfy the no-slip condition at the wall and the acoustic wave solution in the free-stream.

In the downstream limit $x \to \infty$, Eq. (19) has a well known double-layer asymptotic solution that is invariant with the streamwise coordinate, which to leading order[?] is given by

$$u_a = 1 - \exp\left[i^{\frac{3}{2}} \left(\frac{\omega^* x^*}{U_\infty} \right)^{\frac{1}{2}} \eta \right] \ , \tag{21}$$

and represents the so-called Stokes shear-wave layer. In our work, we solve Eq. (19) directly using a space marching finite difference method, and use the above expression merely as a guide to confirm correctness of our equivalent non-parallel numerically computed acoustic solution.

2. Numerical Solution of LUBLE

We solve Eqs. (18) and (19) to second-order accuracy, using upwind finite differences in x with the η-direction discretized using the fully implicit Keller-box method[51]. The steady Blasius state being nonlinear, involves Newton iterations, while the LUBLE being linear in f_a can be solved directly once the steady Blasius solution converges at each x-spatial location during the parabolic numerical marching procedure. Both the Blasius and LUBLE discretizations involve solution of block tridiagonal matrices, which can be accomplished very efficiently using standard LU decomposition. The computational overhead of solving the Blasius and LUBLE equations is negligible compared to the LNS solve steps that we next describe.

C. Steady Mean Flow Distortion Due to Roughness

We consider the presence of a localized roughness element or distributed roughness strip on the flat plate in

the absence of the acoustic wave. The roughness shape is described by $H(x,z)$ while $\hat{H}(x)e^{i\beta z}$ is its Fourier decomposition in the spanwise direction. The small parameter ε_w satisfies $\varepsilon_w = h^*/L << 1$ such that the flow solution can be interpreted as a small perturbation to the base flow varying linearly with ε_w. In these conditions, the governing equations are the steady linearized Navier-Stokes equations. This set of equations is obtained by substituting,

$$\phi(x,y,z) \approx \bar{\phi}(x,y) + \varepsilon_w \phi_w(x,y,z) \ , \tag{22}$$

in Eqs. (1a) and (1b) and linearizing around the base flow, yielding,

$$\vec{\nabla} \cdot \vec{\boldsymbol{v}}_w = 0 \ , \tag{23a}$$

$$\left(\vec{\boldsymbol{v}} \cdot \vec{\nabla}\right) \vec{\boldsymbol{v}}_w + \left(\vec{\boldsymbol{v}}_w \cdot \vec{\nabla}\right) \vec{\boldsymbol{v}} = -\nabla p_w + \frac{1}{R}\nabla^2 \vec{\boldsymbol{v}}_w \ , \tag{23b}$$

where $\vec{\boldsymbol{v}} = [\bar{u}, \bar{v}, \bar{w}]$ and $\partial/\partial t = 0$.

The boundary conditions are written as,

$$\begin{aligned} &\hat{\phi}_w(x, y \to \infty) = 0 \ , \\ &\vec{\hat{\boldsymbol{v}}}_w(x,0) = -\hat{H}(x) \frac{\partial \vec{\boldsymbol{v}}}{\partial y}|_{y=0} \ . \end{aligned} \tag{24}$$

The no-slip condition is satisfied at the wall. In the freestream the flow solution tends towards its unperturbed state.

D. T-S Wave Generation

The highest order term in the double-parameter expansion of Eq. (2) models the viscous instability arising from the non-linear interaction between the steady and acoustic unsteady perturbations as well as from the deformation of the Stokes layer. Through the substitution of Eq. (2) in Eqs. (1a) and (1b) and equating the terms of order $\mathcal{O}(\varepsilon_w \varepsilon_a)$ to zero, the governing equations for determination of the T-S disturbance generation and subsequent evolution are thus of the form,

$$\vec{\nabla} \cdot \vec{\boldsymbol{v}}_c = 0 \ , \tag{25a}$$

$$\begin{aligned} &\frac{\partial \vec{\boldsymbol{v}}_c}{\partial t} - \left(\vec{\boldsymbol{v}} \cdot \vec{\nabla}\right) \vec{\boldsymbol{v}}_c - \left(\vec{\boldsymbol{v}}_c \cdot \vec{\nabla}\right) \vec{\boldsymbol{v}} - \nabla p_c + \frac{1}{R}\nabla^2 \vec{\boldsymbol{v}}_c = \\ &\left(\vec{\boldsymbol{v}}_w \cdot \vec{\nabla}\right) \vec{\boldsymbol{v}}_a + \left(\vec{\boldsymbol{v}}_a \cdot \vec{\nabla}\right) \vec{\boldsymbol{v}}_w \ . \end{aligned} \tag{25b}$$

The right-hand side (rhs) forcing terms represent the interaction between the steady mean flow distorted field (Eq. (23)) and the unsteady acoustic perturbations derived from solving Eq. (19); explicit expressions are detailed in the Appendix. The deformation of the Stokes layer is caused by the presence of the roughness feature and it is mathematically described by the boundary conditions,

$$\begin{aligned} &\hat{\phi}_c(x, y \to \infty) = 0 \ , \\ &\vec{\hat{\boldsymbol{v}}}_c(x,0) = -\hat{H}(x) \frac{\partial \vec{\boldsymbol{v}}_a}{\partial y}|_{y=0} \ . \end{aligned} \tag{26}$$

These wall conditions are found through harmonic balance. In the freestream, far from the surface boundary-layer, the T-S perturbation is assumed to vanish.

III. NUMERICAL APPROACH

Solution of the roughness-induced steady mean flow distortion given by Eq. (23) and subsequent T-S disturbance given by Eq. (25) are accomplished with the same numerical scheme, since the two equation sets have nearly identical form and are of elliptic type.

The wall normal derivatives of the harmonic LNS (see Appendix) are discretized with pseudo-spectral (PS) resolution. The streamwise spatial derivatives are discretized using 4^{th}-order accurate central differences, with non-centered stencils used at the inflow and outflow boundary-points to preserve accuracy. Discretization ultimately yields a large penta-diagonal banded complex matrix inversion problem of the generic form $[\mathcal{L}]\,\tilde{q} = \tilde{r}$; here $\tilde{q}$ is the solution vector for all points in the field and the $\tilde{r}$ vector arises from surface boundary conditions to be satisfied or the coupled wall-acoustic field forcing terms (*i.e* rhs terms of Eq. (25b)). Dimensions of $[\mathcal{L}]$ are $4N_yN_x \times 4N_y(p+1)$, with p representing accuracy order of finite differences (FDs), N_y number of spectral elements and N_x number of streamwise points. Higher order ($p = 6, 8$) finite differences are also possible, but the band-width of the matrices increases thus impacting the LU block factorization CPU time, which increases linearly with N_x and quadratically with band-width $4N_y(p+1)$ increments. The LU decomposition is based on a partially parallelized version of Doolittle's algorithm (OpenMP shared-memory constructs). The work reported in this paper essentially extends Mughal's work[48,52] on development of the harmonic compressible LNS solver.

In the computations we used up to $N_x = 12000$ points in the streamwise direction and $N_y = 56$ PS polynomials. For a specific test case, the inflow plane is located sufficiently far upstream of the roughness such that the perturbations can be considered to be zero there. The outflow plane is positioned downstream of the receptivity region in order to capture the linear growth of the generated T-S wave to allow accurate receptivity amplitude determination; the outflow boundary conditions are based on the PSE radiation condition

$$\frac{\partial \hat{\phi}_c}{\partial x} = i\alpha_p \hat{\phi}_c \ , \tag{27}$$

where α_p is the local streamwise wavenumber computed through a linear PSE computation. Results are checked for convergence with grid refinement and with the position of the inflow and outflow planes.

The efficiency of the technique reported in this paper, which allows the Monte-Carlo UQ analysis to be feasible is based on the crucial observation that the LU decomposition step (the most CPU intensive part of the com-

putation) need only be undertaken once for a prescribed frequency ω and spanwise wavenumber β. With the LU factorization stored in memory, the back-substitutions to solve for parametric variation of the $\tilde{r}$ fields can be accomplished very quickly. Majority of the CPU time ($\sim$ 95%) is used in performing the LU decomposition while the back-solve for a given $\tilde{r}$ vector field is relatively rapid. This was exploited by Mughal & Ashworth[47] in their development of the UQ based methodology to provide variance estimates of the most likely transition location in roughness induced crossflow instability in swept wing flows.

In this paper we use the same strategy, but two LNS solve steps are necessary due to (1) wall roughness $\vec{q}_w$ deformation with $\omega = 0$ and (2) subsequent acoustic-roughness forced LNS solve with $\omega \neq 0$, to give the $\vec{q}_{TS}$ T-S disturbance. This is summarized as follows:

$$\begin{aligned} \vec{\mathcal{L}}_1(\bar{Q};\beta,\omega=0)\vec{q}_w = \vec{r}_w \quad &\rightarrow [L]\,[U]_1\,\vec{q}_w \;= \vec{r}_w \\ \vec{\mathcal{L}}_2(\bar{Q};\beta,\omega)\vec{q}_{TS} = \vec{r}_{aw} &\rightarrow [L]\,[U]_2\,\vec{q}_{TS} = \vec{r}_{aw}. \end{aligned} \tag{28}$$

In the above $\vec{\mathcal{L}}$ matrix dependence on the steady base flow $\bar{Q}$, acoustic frequency ω and spanwise wavenumber β is explicitly stated for elucidation purposes. Hence two LU factorizations $[L]\,[U]_1$ and $[L]\,[U]_2$ require storage in memory; subsequent LU factorizations need only be re-computed for a change in ω or β. On availability of the pre-computed LU factorizations held in memory, the acoustic UQ analysis discussed in this paper may then be undertaken relatively efficiently. Thus, analysis begins firstly by the free-stream acoustic solution (see §II B 2) via the LUBLE for a prescribed ω followed by computation of $[L]\,[U]_1$ and $[L]\,[U]_2$. Finally, for a roughness field $\hat{H}(x)$ prescription the rhs $\vec{r}_w$ vector is constructed, $\vec{q}_w$ solved for and then used in evaluating the $\vec{r}_{aw}$ vector; solution of $\vec{q}_{TS}$ then follows. This may then be repeated multiple times with a new $\hat{H}(x)$ prescription leading through to the $\vec{q}_{TS}$ T-S disturbance evaluation; due to availability of the pre-computed LU factorizations, overhead incurred in the solve steps for multiple realizations of the $(\vec{q}_w, \vec{r}_{aw})$ vectors is thus reduced dramatically.

IV. RECEPTIVITY AMPLITUDE

Receptivity amplitudes are usually expressed in terms of the equivalent amplitude at the lower-branch of neutral stability. This form of presenting the results favors comparability between different approaches and results published in the literature. In this paper we focus on the streamwise velocity disturbance relative to the amplitude of the acoustic wave in the free-stream ($u_{\rm ac} = \varepsilon_a$),

$$\frac{u_{TS}}{u_{ac}} = \varepsilon_w \hat{u}_c(x,y)\;. \tag{29}$$

The linear evolution of the maximum amplitude across the boundary layer with streamwise position x as the disturbance convects is defined by

$$A(x) = \max_y \left(\frac{|u_{TS}(y;x)|}{u_{ac}} \right) \frac{1}{\varepsilon_w}\;. \tag{30}$$

Regardless of the evaluated quantity, the numerical solution is very complex in the near field of the surface roughness feature causing difficulties in estimating the true amplitude of the linear T-S disturbance there. However, downstream of the roughness receptivity region the emergent T-S wave dominates the solution while other non-modal components are damped until they disappear entirely. Therefore, our strategy to extract the T-S wave amplitude at the lower branch of stability is to use a solution of the linear parabolized stability equations (PSE)[22,53] matched near the second-branch of neutral stability with the more correct linear Navier-Stokes prediction. This then allows an accurate determination of the T-S amplitude, *i.e.*

$$A_0 = \frac{A}{e^{-\left(\int_{x_0}^{x} \mathrm{Im}(\alpha) d\xi\right)}}\;, \tag{31}$$

where x_0 is the position where we wish to determine the equivalent T-S wave amplitude. This is often at the neutral stability point or at the surface roughness location. The growth rate $\mathrm{Im}(\alpha)$ derives from the imaginary part of the complex wavenumber α of the T-S wave. In cases where the PSE lack the desired accuracy when compared to the linear-growth predicted by the LNS equations, the latter may be used to generate the linear-growth curve with one extra computation for each frequency. A localized receptivity mechanism positioned upstream of the first-branch of stability is used in this case. This is more costly though and is only used when required.

Goldstein[10] first pointed out that in quasi-parallel receptivity analysis the amplitude of the generated T-S waves could be decoupled from the geometry of the wall feature. Following Choudhari[17] it can be written,

$$\frac{u_{TS}}{u_{ac}} = \varepsilon_w \mathscr{F}\left(\alpha_{TS},\beta\right) \Lambda_u(\omega,\beta,x_r) E(y) e^{i\int_{x_r}^{x} \alpha d\xi}\;, \tag{32}$$

where $\mathscr{F}(\alpha,\beta)$ is the Fourier transform of the wall feature, $\Lambda_u(\omega,\beta,x_r)$ is the efficiency function, $E(y)$ is the normalized eigenfunction such that it is unitary at its maximum, and α_{TS} is the complex T-S streamwise wavenumber at the center of the roughness element x_r. The receptivity amplitude then follows:

$$A_0 = |\mathscr{F}|\left(\alpha_{TS},\beta\right) |\Lambda_u|(\omega,\beta,x_r)\;, \tag{33}$$

and thus allows the efficiency function to be evaluated. Note that because we are working under a non-parallel flow assumption, we need to make sure that the results converge when reducing the width of the roughness element. Non-parallel adjoint approaches typically compute this quantity in the limit of an infinitely thin roughness element[34,54].

For a given combination of free-stream disturbance and wall-inhomogeneity, the efficiency function provides a receptivity measurement that is independent of the local geometry, which thus makes this an appealing measure. Once this has been computed for a set of frequencies of interest, one can instantaneously predict receptivity amplitudes in the presence of localized and distributed roughness with any form, as proposed and discussed by Choudhari[17,18,54]. In the framework of our LNS solver, an efficient computation of the efficiency function can be achieved by storing the LU decomposition in memory, as discussed in Sec. III. Seeing as the LU factorization is the most time-consuming operation, the total computational time to determine the efficiency function for a single frequency and a range of positions x_r can be considerably brought down by performing this step only once. Each roughness configuration then requires a forward and back substitution to obtain the final solution.

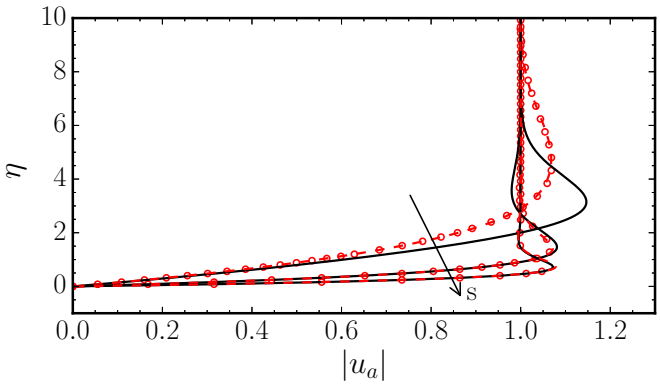

Figure 1. Comparison between linearized boundary layer solver (symbols) and first-order asymptotic solution for high Strouhal number (solid line) for increasing Strouhal numbers $S = \{0.5, 5, 20\}$.

V. APPLICATIONS

In this section we compare the results from the time-harmonic linearized Navier-Stokes approach with other theoretical, experimental and numerical results in the literature. The quite exhaustive checks are used to confirm the correctness of our approach. We then proceed in §VI to investigate acoustic receptivity in the presence of two-dimensional randomly distributed surface roughness fields and quantify the variance arising in receptivity amplitudes. In §VII we demonstrate how the described method may be used to provide quantitative guidance and estimates of the variance in transition location, which naturally arises due to uncertainties in the surface roughness distribution which must exist on real surfaces.

Before we attempt a comparison with other approaches, however, let us first compare the Stokes shear-layer solution obtained with the linearized boundary layer equations against the first-order asymptotic solution in Eq. (21). In Figure 1 we plot the streamwise velocity acoustic perturbation across the boundary layer at different streamwise coordinates. It is shown that near the leading edge, where the Strouhal number $S = x^*\omega^*/U_\infty$ is low, our solution is significantly different than the asymptotic solution for high Strouhal number (as would be expected) and that the two converge further downstream.

A. Saric's Experiment

Saric's flat plate acoustic receptivity experiments[24] consisted of a plane acoustic wave traveling in the streamwise direction and rectangular roughness elements of varying heights placed at a fixed position to generate T-S disturbances of varying magnitude. The rectangular roughness is built with thin Mylar tape placed across the span of a high aspect ratio zero pressure gradient plate. The far-field uniform flow has velocity $U_\infty = 12.75m/s$ and kinematic viscosity $\nu_\infty = 16.84 \times 10^{-6} m^2/s$. The nondimensional frequency of the acoustic wave is set at $F = 2\pi f \nu_\infty / U_\infty^2 = 49.34 \times 10^{-6}$, where f is the dimensional frequency in Hz. The center of the rectangular element is positioned at a distance from the leading edge where the Reynolds number $R_\delta = \left(\frac{U_\infty x^*}{\nu_\infty}\right)^{1/2} = 582$, whereas the T-S wave amplitude is measured at $R_\delta = 1121$ (near the second branch of stability). The measurement is taken at a fixed distance from the wall, namely where the condition $\bar{u}^*(y_M^*)/U_\infty = 0.3$ is satisfied.

The height of the rectangular element is initially 45μm and is incremented by the same amount to a maximum of $315\mu m$. The width is kept fixed at 25mm. Two sound pressure levels of the acoustic wave traveling in the free-stream are tested - $90dB$ and $100dB$. These conditions were reproduced with the methodology presented in Sections II, III and IV. The ratio between the amplitude of the T-S wave and the acoustic wave $|u_{TS}|/u_{ac}$ measured at y_M^* is shown in Figure 2 against the roughness height h^*. The figure compares results from our method against Saric's experiment[24], Choudhari *et al.*[17] and Crouch's[19] quasi-parallel theory. Very good agreement is found between the LNS approach, experiment and local theory, indicating that non-parallel effects are negligible. As mentioned by Choudhari & Streett[17], the fact that the experimental results for $90dB$ and $100dB$ don't agree over the linear regime may be explained by the presence of a T-S wave originating at the leading edge in the absence of the rectangular roughness element. After a certain critical height $h^* > 200$ the phenomena becomes non-linear due to separation of the flow behind the rectangular bump. The experiments for $90dB$ and $100dB$ also don't agree on the critical height leading to a non-linear response, it being lower for the $100dB$ acoustic wave amplitude.

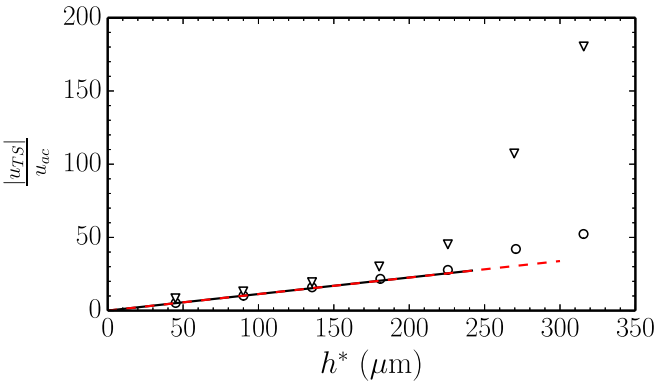

Figure 2. Comparison of Saric's experiment (symbols) with quasi-parallel and non-parallel theories. Solid line - Quasi-parallel theory (Crouch[19] and Choudhari & Streett[17]); Dashed line - LNS; Triangles - 100 dB; Circles - 90 dB

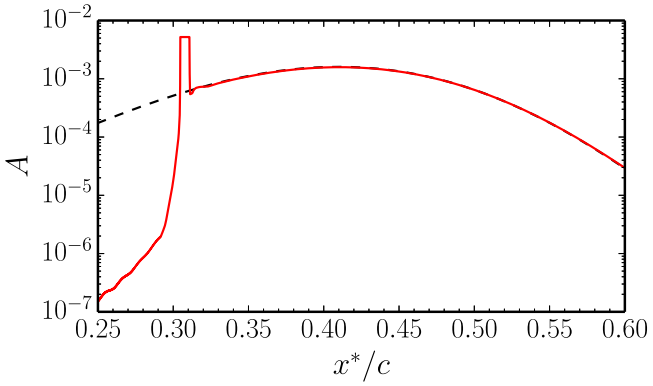

Figure 3. T-S wave development: receptivity and linear growth (A with $\varepsilon_w = 1$ against x^*/c, where c is the chord of the flat plate). Solid line - LNS. Dashed line - PSE. $R_\delta = 1050$, $F = 5 \times 10^{-5}$.

Table I. Receptivity amplitude grid refinement results for $h^* = 300\mu$m.

$N_y = 56$, N_x	1000	1500	2500	5000	7000	10000
$\lvert u_{\rm TS}\rvert/u_{\rm ac}$	64.89	34.45	34.28	34.39	34.50	34.50

$N_x = 7000$, N_y	15	20	30	40	50	56	65
$\lvert u_{\rm TS}\rvert/u_{\rm ac}$	36.96	35.39	34.48	34.57	34.52	34.50	34.51

The LNS computations were performed with 56 Chebyshev polynomials in the wall-normal direction, 7000 points in the streamwise direction, and a domain range $R_\delta = 423$ to $R_\delta = 1197$. In table I we present the results of a grid refinement study. For a fixed value of Chebyshev polynomials $N_y = 56$, the receptivity amplitude varies 0.3% between $N_x = 5000$ and $N_x = 10000$. Conversely, when $N_x = 7000$ the receptivity amplitude varies 0.1% between $N_y = 40$ and $N_y = 65$. Therefore we conclude that $N_x = 7000$, $N_y = 56$ constitutes an adequate choice of grid parameters. We have used very fine grids throughout this work since the computations are not time-consuming. In addition, it allows us to dispel any suspicion that the results might not be converged. In this test-case, for example, there are approximately 200 streamwise points per T-S wavelength. Typically, for a 4^{th}-order accurate finite difference scheme, only 20 points per T-S wavelength are required. In general, a more exacting criterion is to adequately resolve all surface roughness scales. Clearly, for $N_x = 1000$ the rectangular bump is under-resolved, indicating that this value is near the minimum of points required to obtain an accurate solution for this particular application.

B. Localized Receptivity

A more detailed validation of our work is accomplished through the calculation of the efficiency function Λ_u. All computations used a rectangular-shaped bump with constant height $h^* = 1\mu m$. The Fourier transform of a rectangular-shaped roughness element placed at a streamwise position R_δ can be written as,

$$\mathscr{F}(\alpha) = \frac{1}{\alpha}\sqrt{\frac{2}{\pi}}\sin\left(\frac{\alpha d}{2}\right) , \tag{34}$$

where d is the width of the bump. The receptivity amplitude at the center of the roughness element is obtained through Eqs. (30) and (31) using the displacement thickness $\delta_{\rm disp}$ of the boundary layer, at the streamwise position R_δ, as the reference length scale. The efficiency function is then computed with Eq. (33). Results were confirmed to be geometry independent to the desired precision by studying convergence of the results with decreasing width, while numerical independence was ensured with 56 Chebyshev polynomials in the wall-normal direction and 10000 points in the streamwise direction. A typical result of the LNS and linear PSE computation is shown in Figure 3; this also illustrates and confirms the excellent accuracy and thus adequacy of using the PSE based matching procedure to extract the equivalent T-S disturbance amplitude at an upstream position via Eq. (31), as described in §IV.

The LNS computed efficiency function is presented in Figure 4 and compared with results published by Choudhari & Streett's FRNT[17] and Ruban-Goldstein's asymptotic theory[10,11]. Overall good agreement is found between the LNS approach and the FRNT quasi-parallel theory. Non-parallel effects are mostly felt at high frequencies for $R_\delta = 1050$ and at high Reynolds number ($R_\delta > 1300$) for both $F = 20 \times 10^{-6}$ and $F = 25 \times 10^{-6}$. These are confirmed to be qualitatively correct by com-

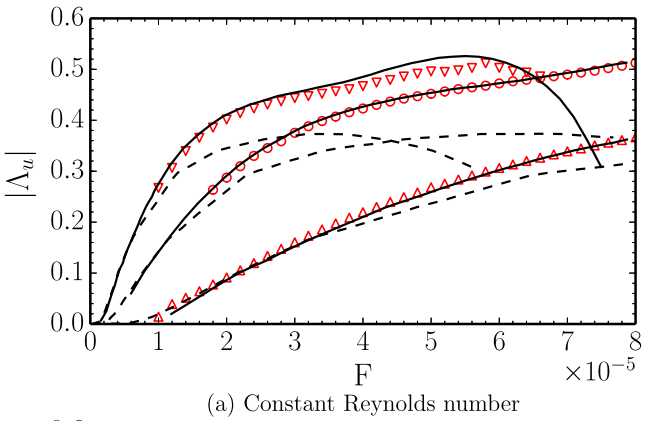

(a) Constant Reynolds number

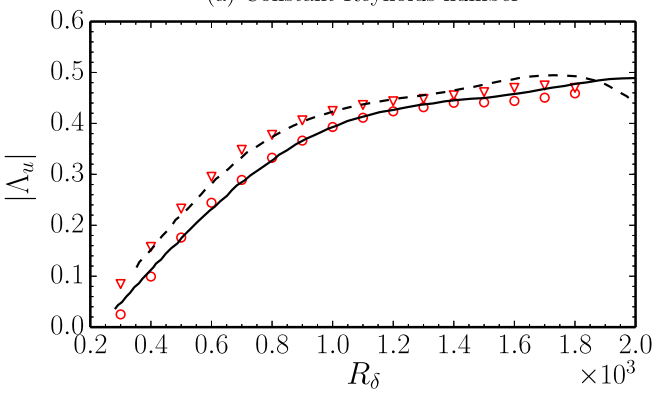

(b) Constant frequency

Figure 4. Efficiency function comparison between three different approaches: asymptotic approach, Choudhari *et al.* quasi-parallel theory and LNS. In figure (a) the asymptotic approach is presented in dashed lines, Choudhari *et al.* in solid lines and LNS in symbols ($R_\delta = 1050$ - downward facing triangles, $R_\delta = 700$ - circles, $R_\delta = 350$ - upward facing triangles). In figure (b) Choudhari *et al.* is presented in lines ($F = 20 \times 10^{-6}$ - solid line, $F = 25 \times 10^{-6}$ - dashed line) and LNS in symbols ($F = 20 \times 10^{-6}$ - circles, $F = 25 \times 10^{-6}$ - triangles).

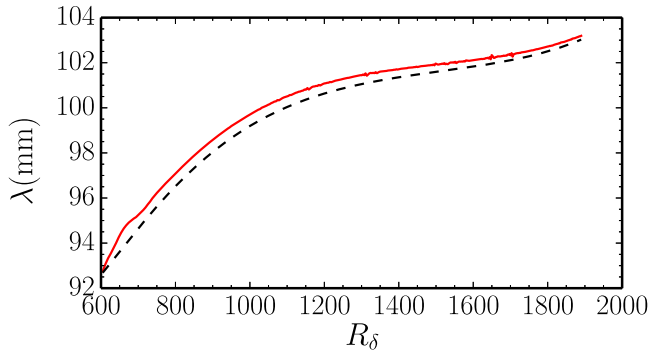

(a) Wavelength

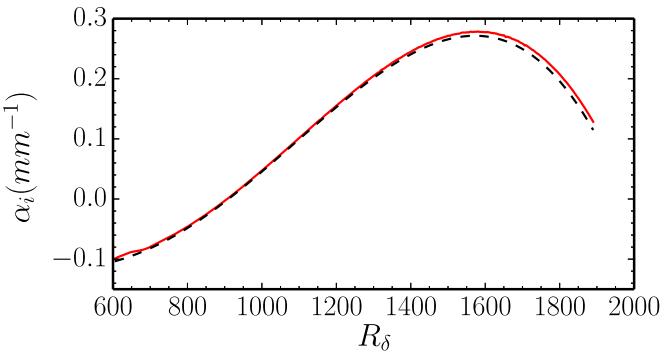

(b) Growth rate

Figure 5. Dimensional wavelength and growth rates of the normal mode from linear stability theory ($F = 25 \times 10^{-6}$). Comparison of PSE (solid line) and Orr-Sommerfeld equation (dashed line).

paring the complex wavenumber of the normal mode calculated through the PSE and the Orr-Sommerfeld equation in Figure 5 for $F = 25 \times 10^{-6}$. Crouch drew the analogue of receptivity as a resonance phenomena of a very complex oscillator[20]. It is known that detuning of the growth rate of the normal mode from the ideal condition $\alpha_i = 0$ has usually a greater impact on the receptivity amplitude and therefore the efficiency function[19]. This is in agreement with what is observed here: the non-parallel results based on the PSE show that above $R_\delta = 1300$ higher growth rates than what is predicted by local theory arise, thus detuning it even further from the ideal resonance condition and therefore leading to a decrease in the efficiency function. This is precisely what is observed in Figure 4, for Reynolds number in excess of 1300. Near the leading edge, *i.e.* at low values of $R_\delta < 400$, non-parallel effects are surprisingly small. This may be due to the fact that though the LNS analysis takes into account both the non-parallel effects on receptivity and on linear growth, they must either counteract each other[38] or be weak enough for FRNT to be still valid.

This comparison has allowed us to validate the time-harmonic LNS approach and we have proven that it predicts the efficiency function accurately, taking into account the non-parallel effects neglected by quasi-parallel theories. At most Reynolds number and frequency parameter F, the agreement with FRNT is remarkably good, though at some (R_δ, F) conditions, differences as high as approximately 10% do arise.

C. Non-localized Receptivity

The time-harmonic LNS formulation is now tested in the presence of distributed roughness. The simplest type is a single-wavelength wavy wall which is historically also the first to have been studied from theoretical[18,20,25] (using quasi-parallel FRNT and asymptotic theory) and experimental viewpoints. Crouch & Bertolotti[21] later extended the quasi-parallel theory to investigate oblique

T-S waves. The wavy wall is described by

$$H = e^{i(\alpha_w^* x^* + \beta_w^* z^*)} \ , \tag{35}$$

where α_w^* and β_w^* are the dimensional streamwise and spanwise wavenumbers. Following Crouch[20], we evaluate the quantity A_0 at the first-branch of stability defined by Eq. (31), with $L = R_f \nu_\infty / U_\infty$, where $R_f = 1000$. Since u_{TS} is known to scale linearly with the wall roughness height, this result is amplitude-independent. The wall wavenumbers are also nondimensionalized with the same reference scale,

$$\alpha_w = \alpha_w^* L, \ \beta_w = \beta_w^* L \ . \tag{36}$$

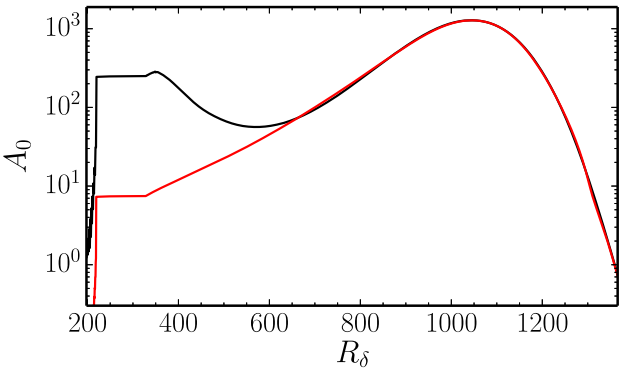

Figure 6. T-S wave evolution for $\beta = 0.1$, $\alpha_w = 0.170$, and $F = 56 \times 10^{-6}$. Red line - waviness extends from $R_\delta = 220$ to $R_\delta = 1300$. Black line - a localized receptivity mechanism was placed at $R_\delta = 220$ and the curve was matched with the red curve at the second branch of stability.

The grid used 12000 points in the streamwise direction and 56 Chebyshev polynomials in the wall-normal direction. The computational domain extends from the leading edge to $R_\delta = 1400$. The wall waviness extends from $R_\delta = 220$ to $R_\delta = 1300$. Crouch[19] found that receptiveness is maximized around the lower-branch of stability and rapidly diminishes with streamwise extent away from this point; *i.e.* the energy transmission from the forced mode to the eigenmode quickly decreases to zero as the detuning from the resonance conditions increases away from the neutral point. Therefore, after a certain distance, the fully developed growing in amplitude T-S disturbance no-longer feels the presence of the wavy wall forcing and continues its development according to linear eigenmode theory. This is illustrated in Figure 6. The perturbation, in red, becomes a pure T-S wave at approximately $R_\delta = 900$ in spite of the presence of waviness until $R_\delta = 1300$. The equivalent amplitude A_0 is measured at the lower-branch of neutral stability through the black curve.

The T-S wave amplitudes for $F = 56 \times 10^{-6}$ and varying wall waviness wavelength are presented in Figure 7. Comparisons are made with Crouch's quasi-parallel theory both for two and three-dimensional disturbances[20,21]. Additionally, results from the multiple-scales non-parallel two-dimensional disturbance analysis of Zuccher[31] are presented. This allows us to confirm and contrast the more *exact* and flexible LNS modeling capability investigated by us with the multiple-scales based results.

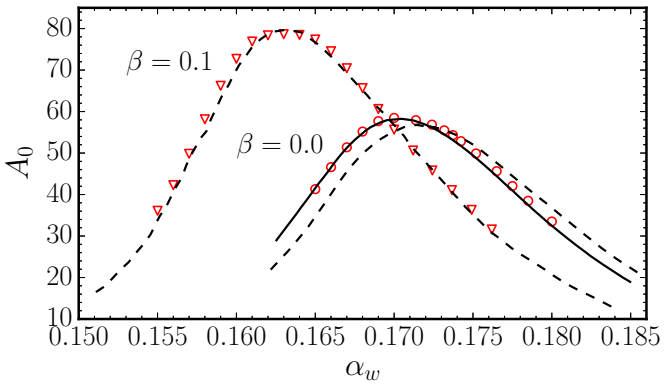

Figure 7. Wavy wall receptivity amplitudes as a function of the streamwise wall wavenumber for $\beta = 0.0$ (dashed line - Crouch's quasi-parallel theory[20] - , solid line - Order one multiple scales approach[31], symbols - LNS) and $\beta = 0.1$ (dashed line - Crouch et al. quasi-parallel theory[21] - and symbols - LNS) ($F = 56 \times 10^{-6}$).

As alluded to already, receptivity is at its core a resonance phenomena between the external forcing and a very complicated oscillator. The wavy wall test case illustrates this quite well. Only in a short interval of wavelengths is the wall waviness effective in generating T-S disturbances. The T-S amplitudes quickly decrease to zero away from this optimal region. For a given acoustic frequency, this most receptive band of wavelengths is determined by the characteristics of the corresponding eigenmode, which can be obtained through spatial stability analysis. Ideally one would have

$$\alpha_w = \alpha_{TS}^r, \ \alpha_{TS}^i = 0 \ , \tag{37}$$

where the superscripts r and i stand for real and imaginary parts respectively. However, because this is a non-localized phenomenon and the T-S wavelength changes as it convects, neither condition can be met at all streamwise coordinates. Non-satisfaction of the second condition is a more effective detuning mechanism and leads to lower receptivity amplitudes[20].

For the two-dimensional test case ($\beta = 0$) very good agreement is found between the LNS approach and the multiple scales approach. Discernible non-parallel effects can be noted when comparing with Crouch's local theory; a shift in most effective surface waviness wavelength and an increase in amplitudes are observed. On the other hand, the three-dimensional test case ($\beta =$

0.1) reveals good agreement between the non-parallel LNS theory and Crouch's quasi-parallel theory. Crouch & Bertolotti[21] had reported that "linear-growth rates of three-dimensional disturbances are more strongly affected by non-parallelism." As mentioned earlier, in context of localized roughness, non-parallel effects quantified by our LNS computations are the net contribution from both the receptivity process and subsequent linear development of the T-S disturbance. As such, it appears reasonable to conclude that what we observe for the $\beta = 0.1$ oblique 3D-disturbance, is a near-perfect cancellation of two contrary effects. The same may not happen however, for all spanwise wavenumbers or for alternate steady base flows.

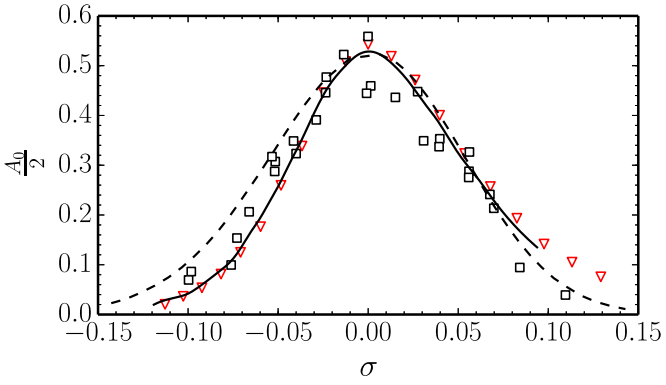

Figure 8. Wavy wall receptivity amplitude as a function of the detuning parameter $\sigma = \alpha_w/\alpha_m - 1$. Comparison of LNS (triangles) with Wiegel & Wlezien's experiment[26] (squares), FRNT theory of Choudhari[18] (solid line) and Wu's first-order asymptotic theory[25] (dashed line).

Experimental validation of Choudhari[18] and Crouch[20] FRNT-based wavy-wall predictions were undertaken by Wiegel & Wlezien[26]. Wall waviness was reproduced through a series of $40\mu m$-thick polyester tape spaced $25.4mm$ apart ($50.8mm$ center to center) up to a total of 13 strips. As seen in Figure 7, for a given frequency there is a very narrow band of wall wavenumbers for which resonance occurs and instabilities with non-negligible amplitude appear. This property aided Wiegel & Wlezien to use periodically placed rectangular roughness shapes (the first Fourier component has a wavelength of $50.8mm$ while the next harmonic is three times smaller and therefore already sufficiently out of tune to be neglected). The uniform free-stream speed was $12.5m/s$ while a plane acoustic wave with a frequency of $80Hz$ was forced. Although not explicitly stated in the original work, Wu[25] deduced from the data that the kinematic viscosity, based on a temperature of about $25°C$, was $\nu_\infty = 1.546 \times 10^{-5} m^2 s^{-1}$.

The 2-D wavy wall is described with Eq. (35), where $\alpha_w^* = (2\pi/0.0508)\ m^{-1}$. The dimensional amplitude of the wavy wall is $h^* = (20 \times 4/\pi)\ \mu m$ (half the height of the rectangular tape strips times the Fourier series coefficient). The LNS grid used 10000 points in the streamwise direction and 56 Chebyshev polynomials in the wall-normal direction. Wall waviness was prescribed from $R_\delta = 140$ to $R_\delta = 1600$, while the entire computational domain extended from the leading edge to $R_\delta = 1800$. The evaluated quantity is $A_0/2$. A factor of $1/2$ appears because we use a complex description of the wall waviness instead of a real sinusoidal function.

A direct comparison of our computations with Wiegel & Wlezien's[26] results is presented in Figure 8. Amplitudes are plotted against the detuning parameter $\sigma = \alpha_w/\alpha_m - 1$, where α_m corresponds to the wavenumber for which the receptivity coefficient is maximal. First-order asymptotic theory results of Wu[25] and FRNT results of Choudhari[55] are also superimposed. Wu attempted a second-order correction to his leading-order results, but the corrections significantly over-predicted the receptivity amplitudes compared to FRNT and experiments (see Figure 9 of Wu), and are thus not presented here. Wu attributed this discrepancy to the possibility of small mean flow pressure gradients in the experiment, which would have resulted in significantly different N-factors, not accounted for in Wiegel & Wlezien's experiment post-processing. The results obtained with the LNS approach however indicate that this is not the case. Moreover, it is observed that the non-parallel flow effects are small and mostly felt for positive values of the detuning parameter, reaching approximately 10%. Overall, very good agreement is found between the finite-Reynolds number theory, LNS and the experiment.

Above, we have shown our proposed LNS approach produces accurate results both for localized and non-localized idealized wall roughness through comparisons with theoretical, numerical and experimental works. Having undertaken quite detailed validations of the new approach described in this paper, we next consider the more practical case of how we can incorporate and develop a T-S receptivity method to account for the effects of realistic rough surfaces, which have an element of randomness in the roughness field description.

VI. DISTRIBUTED RANDOM ROUGHNESS

Wing manufacturing processes are inherently imperfect. Surfaces can never be smooth, possessing irregularities over a wide range of wavelengths[56]. The height distribution in relation to a mean plane has been observed to be a non-stationary random process[56]; therefore the variance of the height distribution is usually dependent on the sample length. Moreover, the work of Majumdar & Tien[57] highlights that beyond a certain surface roughness scale, surfaces may be characterized by self-similarity and self-affinity properties related to fractal behavior, where similar geometric patterns are found at different scales.

Predicting receptivity amplitudes in the presence of random distributed roughness is a key step towards

practical transition prediction on an otherwise assumed *smooth* surface. The study of acoustic receptivity in the presence of localized roughness and wavy walls can be regarded as a cornerstone to understand the physics and study of the more general problem of continuous and discrete spectrum surface features. Choudhari[18] addressed this problem although he did not proceed to study any particular roughness distributions. This was done for stationary cross-flow instabilities over swept wings by Mughal & Ashworth[47] and Thomas *et al.*[37] The former work reconstructed the power spectral density (PSD) of a painted panel and an unpainted aluminum plate and showed that energy tends to be concentrated in the small wavenumbers. To overcome the issues of randomness existing in the surface roughness field distribution and spectral content description, Mughal & Ashworth[47] used a Monte-Carlo (MC) based uncertainty quantification analysis in their receptivity modeling. The premise, which was verified, is that over a large number of surface roughness realizations the receptivity amplitude will converge to a mean value and will have an associated variance which ultimately leads to uncertainty in the transition location. In a real surface, the sources of uncertainty are the variations in the PSD functions in different parts of the surface and in relative phase of the different Fourier components. However, to the best of our knowledge, no equivalent studies have been conducted on the generation of Tollmien-Schlichting waves; T-S receptivity has the added complication of uncertainties and randomness existing in the freestream acoustic environment too. A key motivation of this paper is to address and devise an appropriate high-fidelity methodology to overcome this current limitation in T-S induced transition modeling.

A. Surface Roughness Model

In this section we will focus on the two-dimensional model,

$$H^*(x) = k_{\text{rms}} \sum_{i=N_{\text{min}}}^{N_{\text{max}}} a_i \cos\left(\frac{2\pi i x}{\lambda_x} + \phi_i\right) , \tag{38}$$

where a_i follows a Gaussian distribution with mean

$$\mu_i = \left(\frac{2\pi i}{\lambda_x}\right)^{-k} , \tag{39}$$

and standard deviation

$$\sigma_i = \frac{k_\sigma \mu_i}{3} . \tag{40}$$

The length of the roughness patch is denoted λ_x. A phase ϕ_i for each mode is sampled uniformly from the interval $[-\pi, \pi]$. The Fourier series is cut-off by low and high-pass filters denoted N_{min} and N_{max} respectively. The low-pass filter is determined by the maximum sample length (λ_s) with which we can characterize the surface roughness – $N_{min} = \lambda_x/\lambda_s$. The high-pass filter is conditioned by the finest scales relevant to the physical phenomenon under study.

Each roughness spectral scale is attributed a random amplitude a_i. The mean PSD follows a power law, which has been observed to be a good fit to natural random roughness[56–58]. In particular, Van Deusen[58] observed a decay with the square of the angular frequency for many different types of surfaces. Majumdar & Tien[57] noted, however, that machined surfaces may present two distinct behaviors throughout the spectrum: (i) a first power law at low wavenumbers with a slope in a log-log plot which is defined by the surface-processing technique, (ii) followed by a second power law with a different slope at the high-wavenumber end of the spectrum. The two branches intersect at a so-called corner wavenumber. The authors proposed that this wavenumber is determined by the smallest scale at which the machine can effectively process the surface. At finer scales the surface roughness remains unprocessed. This aspect is not considered in the present work.

In order to relate our power law coefficient k to previous works[58] we first calculate the autocorrelation of our model ($\phi_i = 0$ for simplicity and $k_\sigma = 0$),

$$\begin{aligned} R(\tau) &= \lim_{L\to\infty} \frac{1}{L} \int_0^L H(x) H(x+\tau) dx \\ &= \frac{k_{\text{rms}}^2}{2} \sum_{i=N_{\text{min}}}^{N_{\text{max}}} \mu_i^2 \cos\left(\frac{2\pi i \tau}{\lambda_x}\right) . \end{aligned} \tag{41}$$

The power spectrum then follows as the Fourier transform of the autocorrelation function,

$$S(\alpha_w) = \frac{k_{\text{rms}}^2}{2} \sum_{i=N_{\text{min}}}^{N_{\text{max}}} \mu_i^2 \delta(\alpha_w - \frac{2\pi i}{\lambda_x}) . \tag{42}$$

The amplitudes of the discrete power spectrum of the Fourier series behave with the same power law as its continuous approximation[59]. Therefore, to obtain the decay with the square of the angular frequency found by Van Deusen[58] we must use $k = 1$.

The standard-deviation, in its turn, is tuned through k_σ, which represents the percentage around the mean value in which 99.73% of all roughness realizations will be contained. During a Monte-Carlo simulation, each realization of the roughness field is kept at a constant root-mean-square (r.m.s.) height through the scaling coefficient k_{rms}. This quantity has been observed to be nearly constant in natural and artificial roughness surfaces[57]. It depends, however, on the length of the considered sample. The r.m.s height is defined as,

$$h^*_{\text{RMS}} = \sqrt{\frac{1}{\lambda_x} \int_0^{\lambda_x} {H^*}^2(x) dx} . \tag{43}$$

which coincides with the definition of standard-deviation for a height distribution with a mean plane placed at $y = 0$.

Admittedly, this model lacks the properties of self-similarity and self-affinity present in Majumdar & Tien's model[57]. On the other hand, unlike the Weierstrass-Mandelbrot fractal function presented in their work, it possesses the necessary spectral density to capture the receptivity phenomenon in the range of wavelengths which are most likely to generate T-S disturbances.

B. Surface Roughness Characterization

Let us consider a roughness patch of length $\lambda_x = 1.0$ and a surface roughness sample of length $\lambda_s = 0.1$, with the chord of the flat plate as a reference length scale. The low-pass filter is then $N_{\min} = 10$ and we specify $N_{\max} = 1000$, $k = 1$ and $k_\sigma = 0.0$. The scaling parameter k_{rms} is such that $h^*_{\text{RMS}} = 20\mu m$. Figure 9 shows an example of a roughness realization with this parametrization. In Figure 10 we confirm that this model generates randomized roughness with a height distribution which follows a Gaussian law to a good degree of approximation[57].

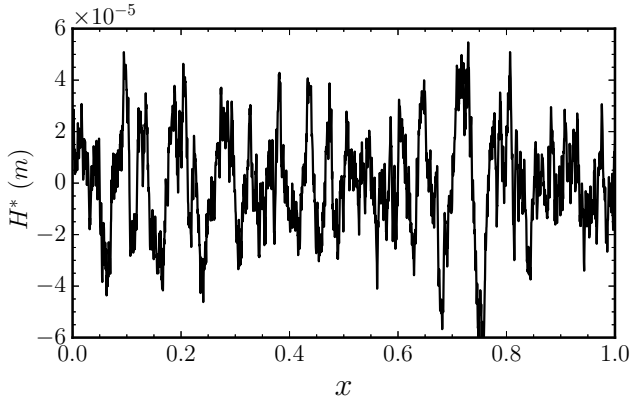

Figure 9. Example of a roughness patch.

When generating a large number of roughness patches we observe that the mean plane is consistently positioned at $H^* = 0.0$ and that the variance of the height distribution is constant. This means that the r.m.s is constant which is another observed property of natural and artificial roughness surfaces. Figure 11 presents an example of the PSD, subject to uncertainties modeled through a Gaussian distribution with an associated variance defined by $k_\sigma = 0.5$. In black we show the mean PSD decays with the square of the wavenumber α_w.

C. T-S Disturbance Generation

We next focus on the generation of two-dimensional T-S waves in the presence of 2D random distributed roughness following the aforementioned model. The global Reynolds number based on chord and the root-mean-square height were kept constant - $R = 3.2 \times 10^6$, $h^*_{\text{RMS}} = 1\mu m$. The low-pass filter is set at $N_{\min} = 10$ with a roughness patch extending through to 90% of the plate length ($\lambda_x = 0.9$, $x^*/c = x \in [0, 1]$). Roughness strips are arranged to start close to the leading edge of the flat plate, within the stable regime of the neutral stability diagram, to ensure that the receptivity phenomenon is fully captured. The dependence of the receptivity amplitudes on the roughness strip length is well known to converge to a constant value for a sufficiently long strip[21,47]. This is discussed and confirmed in the wavy-wall test case of §V C and related result shown in Figure 6.

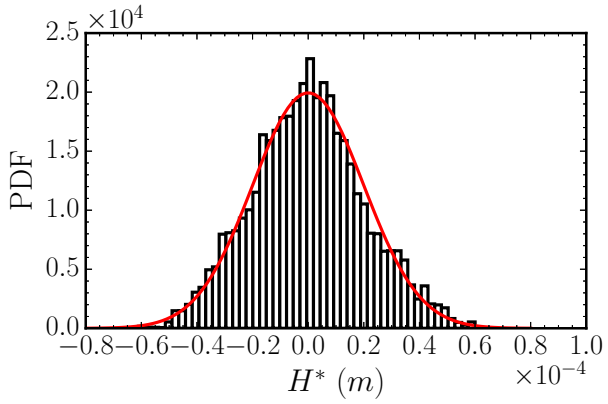

Figure 10. Normalized probability density function of the height distribution of a roughness patch.

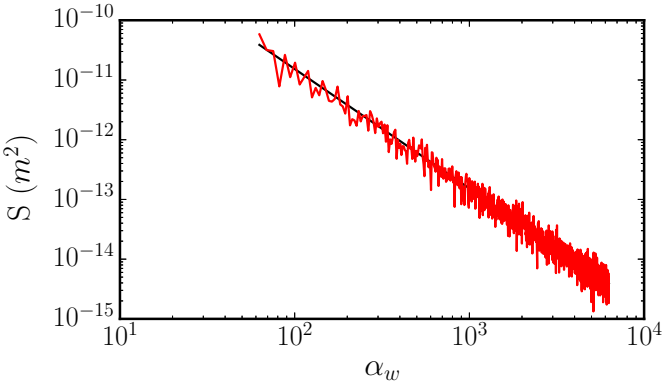

Figure 11. Example of a randomized PSD (in red) superimposed on the mean PSD (in black) - $k_\sigma = 0.5$.

All computations used 10000 points in the streamwise direction and 56 Chebyshev polynomials in the wall-normal direction. The large point distribution thus ensured that all fine roughness scales (*i.e.* constrained by N_{max}) were resolved in the numerical discretization of the simulated roughness field; ramifications of under-resolving the roughness scales is discussed in some detail by Thomas *et al.*[37] Receptivity amplitudes are calculated at the lower-branch of neutral stability according

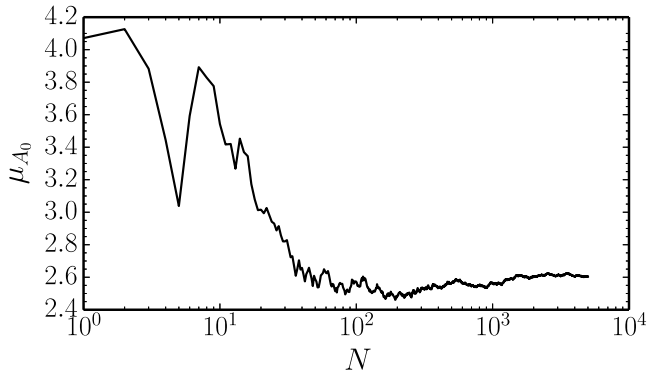

(a) Mean receptivity amplitude plotted against the iteration number N

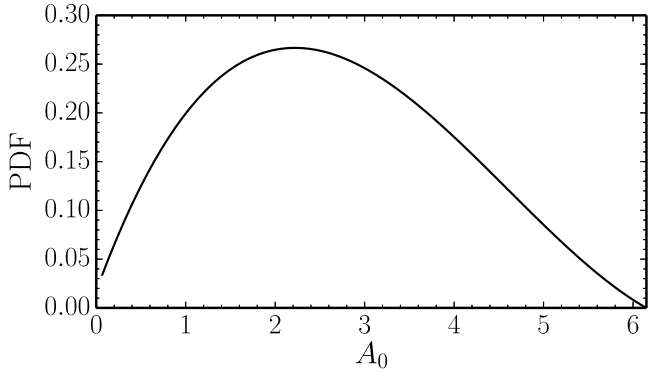

(b) Probability density function

Figure 12. Monte-Carlo simulation with parameters $k = 1$, $k_\sigma = 0.0$, $N_{\max} = 500$ and $F = 56 \times 10^{-6}$.

to Eq. (31), where $h^* = \sqrt{2}h^*_{\text{RMS}}$ is the amplitude of a wavy wall for a given r.m.s height. The reference length scale is $L = R_f \nu_\infty / U_\infty$, with $R_f = 1000$ to maintain comparability with the wavy wall results. The minimum wavenumber of the roughness grain sizes (wavelengths) under this scaling is $\alpha_{\min} = 0.0218$.

Let us first consider an acoustic wave traveling in the freestream with non-dimensional frequency $F = 56 \times 10^{-6}$. The PSD is invariant ($k = 1$, $k_\sigma = 0.0$) and the high-pass filter is set at $N_{\max} = 500$. The maximum wavenumber is then $\alpha_{\max} = 1.091$. The range of roughness wavenumbers ensures that the relevant scales associated with the analyzed acoustic wave frequencies are present. Figure 12(a) shows the evolution of the mean receptivity amplitude, $\mu_{A_0} = E[A_0]$, against the number of random roughness realizations N. Convergence towards a constant mean amplitude is confirmed. Moreover, observe that convergence is attained with approximately 3000 roughness field realizations. Consequently, in all subsequent computations the number of roughness realizations is fixed at 3000. The corresponding probability density function is presented in Figure 12(b).

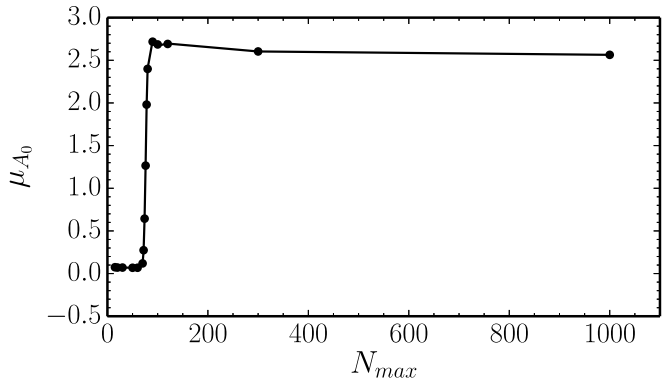

Figure 13. Mean receptivity amplitude against the low-pass filter wavenumber - $k = 1$, $k_\sigma = 0.0$, and $F = 56 \times 10^{-6}$

Having verified the core premise of the uncertainty quantification analysis technique, we next analyze the influence of the described parameter set. Firstly, we maintain the parametrization while increasing $N_{\max}$, thus including finer and finer scales – results are shown in Figure 13. Since the acoustic frequency is kept constant, it is well known that the range of wavenumbers for which the resonance conditions are met is very narrow. Consequently, when only large scales are present, the receptivity amplitude is near-zero. As we start to include the relevant scales in the random roughness, the amplitude quickly increases, reaching a peak value and then decreasing mildly towards a constant value. The reason for this decrease is that maintaining a constant roughness r.m.s height, and therefore a constant forcing *energy* at the surface, means that the broader the roughness spectrum is, the most effective roughness scales (from a resonance viewpoint) have reduced impact since the r.m.s measure is shared more evenly over the roughness spectral content. However, since the power density decays very rapidly with the wavenumber (see Figure 11), an almost negligible contribution arises from the very fine scales.

The behavior with varying $N_{\min}$ is predictable provided it is sufficiently low so as to include the relevant scales for the receptivity phenomenon. For $F = 56 \times 10^{-6}$, it has to be lower than approximately 60 as can be confirmed through Figure 13. If, however, it were lower than the value we have used in this test case, we would see a generalized decrease in T-S wave amplitudes simply due to the fact that more of the irrelevant length scales are assigned non-zero magnitude, leading to assignment of reduced roughness amplitudes to the more effective roughness scales.

Thus far the analysis has shown that for a sufficiently large number of roughness realizations we are capable of finding a PDF for the T-S wave amplitude at the lower branch of neutral stability with a well defined mean and

variance. Moreover, we have observed that the average receptivity amplitude converges to a constant value when increasing the parameter $N_{\max}$. In what follows we investigate the effects of the non-dimensional frequency F, the power law coefficient k and the power law variance coefficient k_σ. Frequency is varied in the range $[24, 80] \times 10^{-6}$ while $k = \{0.75, 0.9, 1.0, 1.05\}$ and $k_\sigma = \{0.0, 0.25, 0.50, 0.75\}$. The high-pass filter is kept constant at $N_{\max} = 500$.

The variation of the mean receptivity amplitude and variance with the non-dimensional frequency and the parameter k is presented in Figure 14. The mean receptivity amplitude is weakly dependent on the frequency of the acoustic forcing. For $k = 0.9$ it is nearly constant. For lower k values there is an increase in amplitude with increasing frequency. Conversely, for steeper PSD's, we see a decrease of amplitudes with frequency. This can be explained if we consider that for each acoustic wave frequency, the most favorable wall roughness wavelengths that are most effective in generating the T-S disturbance are confined to a very narrow band (see §V C). Moreover, these relevant scales become increasingly small with increasing frequency. Figure 11 shows that these wavenumbers have less associated energy. Therefore, this effect promotes a decrease in receptivity amplitude with the acoustic forcing frequency. However, one must also consider the efficiency of the receptivity process at each frequency when all roughness scales have the same magnitude. The fact that for $k = 0.75$ we observe an increase in amplitude indicates that the efficiency of the process increases in this range of frequencies. It is only when we impose a steeper decrease of energy density with the wavenumber of the roughness (*i.e.* when we increase the parameter k) that we see the first effect we described dominating the general trend.

Secondly, we observe that the variance follows similar trends and is comparable in value to the mean T-S wave amplitude. This indicates that the 95% confidence interval is very wide - see Figure 12(b). The disparity in receptivity amplitudes at the first-branch of stability is caused almost exclusively by differences in phase of each component of the randomized roughness model. Since the process is entirely linear, the resulting T-S wave can be seen as the sum of the T-S waves emanating from each wavy wall of wavenumber $2\pi i/\lambda_x$. The relative phases of the partial T-S waves will then either promote constructive or destructive interference. This explains why a T-S wave amplitude can go from near-zero to twice as much as its average amplitude.

Lastly, we consider the effect of random variations in the PSD. In Figure 15 the power law coefficient is fixed to $k = 0.75$ and $k_\sigma = \{0.0, 0.25, 0.50, 0.75\}$. We observe that the mean amplitude and the variance remain nearly unchanged. Small variations arise but these can be mostly attributed to statistical errors. These results support the idea that the phase differences between each wavy wall component of the random roughness largely determine the PDF of the T-S wave amplitude.

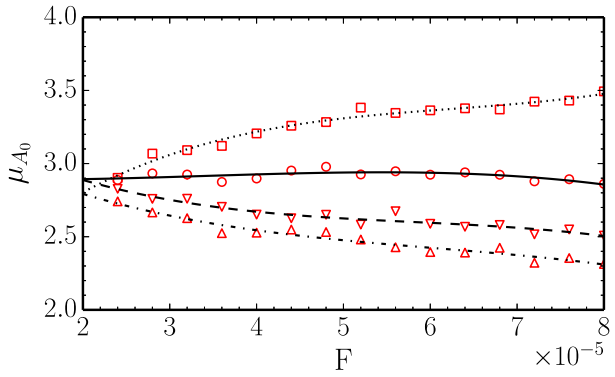

(a) Mean receptivity amplitude

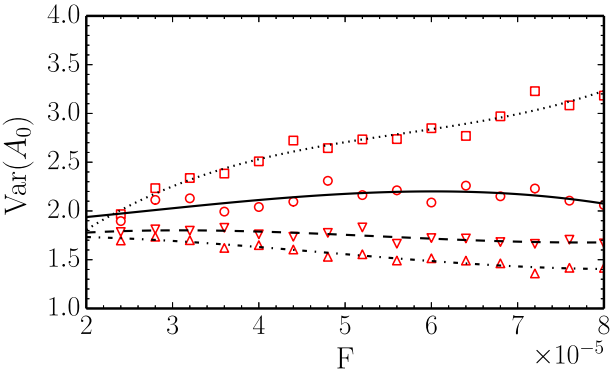

(b) Receptivity amplitude variance

Figure 14. Receptivity to different acoustic wave frequencies and power spectral densities of the random distributed surface roughness ($N_{\max} = 500$, $k_\sigma = 0.0$). Squares - $k = 0.75$, Circles - $k = 0.9$, Downward facing triangles - $k = 1.0$, Upward facing triangles - $k = 1.05$

VII. T-S WAVE GROWTH AND TRANSITION LOCATION

Receptivity models such as the one presented in this paper provide us with initial amplitudes of boundary layer instabilities which subsequently undergo exponential growth. If these linear disturbances become sufficiently large, they generate and interact with subharmonics in a non-linear growth process. Eventually the disturbances become of the order of the base flow quantities, which leads to the generation of secondary instabilities. Breakdown to transition should follow very quickly[22]. This transition scenario is valid in a small perturbation environment.

We next demonstrate, relying on the initial amplitudes calculated in the previous section, how we can simulate T-S wave growth and also provide indications of the likely variances to expect in the nonlinear breakdown position. For this we use the non-linear parabolized stabil-

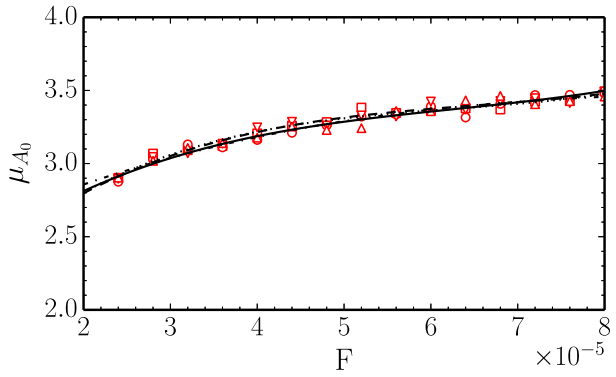

(a) Mean receptivity amplitude

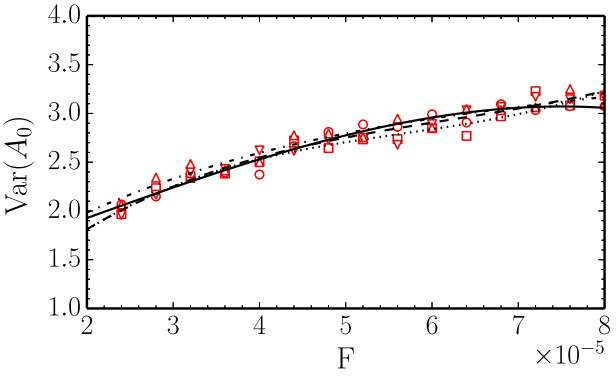

(b) Receptivity amplitude variance

Figure 15. Receptivity to different acoustic wave frequencies and power spectral densities of the random distributed surface roughness ($N_{\max} = 500$, $k = 0.75$). Squares - $k_\sigma = 0.0$, Circles - $k_\sigma = 0.25$, Downward facing triangles - $k_\sigma = 0.5$, Upward facing triangles - $k_\sigma = 0.75$

ity equations (NLPSE)[22,60]. These equations are valid until the instabilities become $\mathcal{O}(1)$, at which stage convergence problems arise in the NLPSE's numerics. We assume that the point of numerical non-convergence heralds the onset of imminent breakdown to turbulence; we define this as a good indicator of transition location. Each frequency is treated independently, as if the acoustic disturbance spectrum in the freestream were dominated by a single acoustic wave of frequency F. Therefore the sub-harmonics generated during the NLPSE solution evolution have a zero initial amplitude, and we limit the NLPSE computations to self-generate only four sub-harmonics. Using a larger number of sub-harmonics has little effect on the results presented.

Hereafter we seek to assess the effect of the uncertainty in the initial T-S wave amplitude on transition location. We are aware that the non-linear process leading to breakdown into turbulence is ultimately a three-dimensional phenomenon involving interaction between the dominant T-S wave and three-dimensional modes – examples include 'K-type' and 'H-type transition[22,61]. Accurately predicting this behavior would require using a 3-D roughness model to obtain the initial amplitudes of oblique modes or equivalent 3D acoustic forcing. We restrict our analysis to two-dimensional disturbances for the purpose of illustrating how the receptivity model can be coupled with the NLPSE to predict breakdown into turbulence.

The initial amplitude at the lower-branch of stability is calculated according to

$$u_{\mathrm{TS}} = \frac{\varepsilon_a \sqrt{2} h^*_{\mathrm{RMS}}}{L} \left(\mu_{A_0} + n\sigma\right) \tag{44}$$

where n is an integer, $\sigma = \sqrt{\mathrm{Var}(A_0)}$, and $L = R_f \nu_\infty / U_\infty$ is the reference length scale; non-zero n allows the effect of uncertainty to be quantifiable. In what follows the unit Reynolds number is 658400, $k = 1$, and $k_\sigma = 0$.

Figure 16 presents the results for an acoustic wave amplitude $\varepsilon_a = 1 \times 10^{-4}$, roughness r.m.s. $h^*_{\mathrm{RMS}} = 20\mu m$, and $n = 0$ (average receptivity amplitude). The dashed vertical line marks the Reynolds number at which the most unstable T-S wave reaches an amplitude of approximately 10% of the freestream velocity – $R_\delta = 1834$. At this point the NLPSE computation breaks down. For this particular scenario it corresponds to the frequency $F = 28 \times 10^{-6}$.

The envelope in Figure 16 also provides information as to which roughness lengthscales should be suppressed, or at least mitigated, in order to delay the onset of strongly nonlinear instabilities. In this case lowering the initial amplitudes of T-S disturbances with frequencies below $F = 28 \times 10^{-6}$ could well delay the breakdown to turbulence altogether. These T-S waves, in turn, are most receptive to roughness with a wavenumber lower than 0.12 (long wavelengths).

Since the variance of the T-S wave initial amplitude due to the stochastic nature of the roughness field is comparable to the its mean value, we re-perform the NLPSE computations for $n = -2$ and $n = 2$. In Figure 17 we only present the most dangerous frequency for each value of n. When $n = 2$ receptivity amplitudes are at the high-end of the PDF and naturally the instabilities become $\mathcal{O}(1)$ further upstream ($R_\delta = 1725$). The contrary effect is observed when $n = -2$ ($R_\delta = 2300$). The Reynolds number variation with respect to the mean value is greater for the latter case, *i.e.* a relatively larger shift downstream in transition location arises for $n = -2$ variance, while lesser sensitivity in the upstream transition location movement is observed with the $n = 2$ variance. Note also how the increase in initial amplitudes is directly linked to an increase in frequency of the most dangerous mode.

If we consider that the boundary layer is being excited by an acoustic field with a single frequency $F = 28 \times 10^{-6}$, we can deduce from Figure 17 that transition should not occur before $R_\delta = 1725$. It can, however, occur further

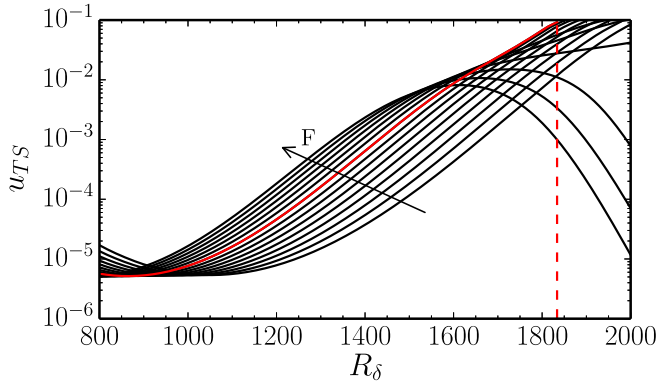

Figure 16. NLPSE simulation of T-S wave growth for $\varepsilon_a = 1\times 10^{-4}$, roughness r.m.s. $h^*_{\rm RMS} = 20\mu m$. Frequencies ranging from $F = 20\times10^{-6}$ to $F = 34\times10^{-6}$. Red curve corresponds to $F = 28\times10^{-6}$, which is the first T-S wave to attain a near 10% amplitude.

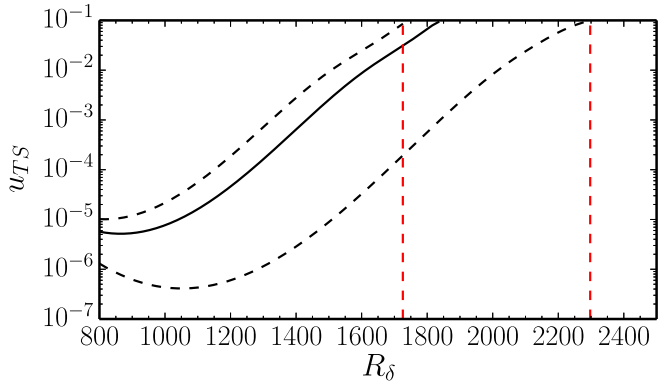

Figure 17. NLPSE simulation of T-S wave growth for $\varepsilon_a = 1\times10^{-4}$, roughness r.m.s. $h^*_{\rm RMS} = 20\mu m$. From right to left in the graph - $n = \{-2, 0, 2\}$. The corresponding frequencies are $F = \{20, 28, 31\}\times10^{-6}$.

downstream beyond $R_\delta > 2300$. On average it should be at $R_\delta = 1834$. These variations would be caused solely by the stochasticity of the roughness field.

In Figure 18 we present similar analysis with a smoother roughness field. The r.m.s. was reduced by a factor of 10. No curve for $n = -2$ is presented as none of the acoustic wave frequencies excite a T-S wave that attains an $\mathcal{O}(1)$ amplitude (within the computational domain considered). Note how the transition Reynolds numbers for $n = \{0, 2\}$ move downstream relative to the results presented in Figure 17.

Lastly, in Figure 19 the acoustic wave amplitude is increased tenfold while maintaining the r.m.s. at its reference value $h^*_{\rm rms} = 20\mu m$. An overall increase in receptivity amplitudes clearly promotes earlier transition, although other trends remain identical. The most dangerous frequencies grow with the initial T-S wave amplitude – both for $n = \{-2, 0, 2\}$ in Figure 19 and in relation to Figure 17.

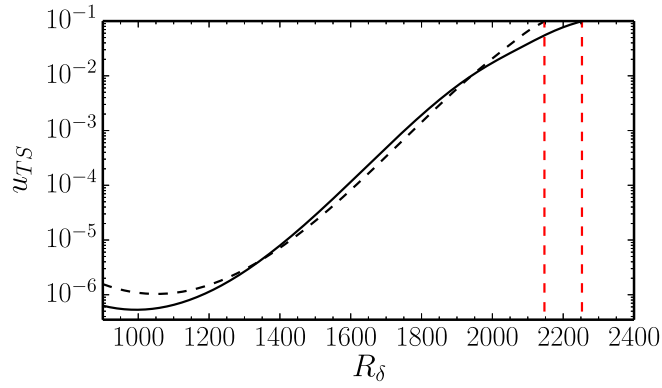

Figure 18. NLPSE simulation of T-S wave growth for $\varepsilon_a = 1\times10^{-4}$, roughness r.m.s. $h^*_{\rm RMS} = 2\mu m$. Solid line - $n = 0$ and $F = 22\times10^{-6}$; Dashed line - $n = 2$ and $F = 20\times10^{-6}$.

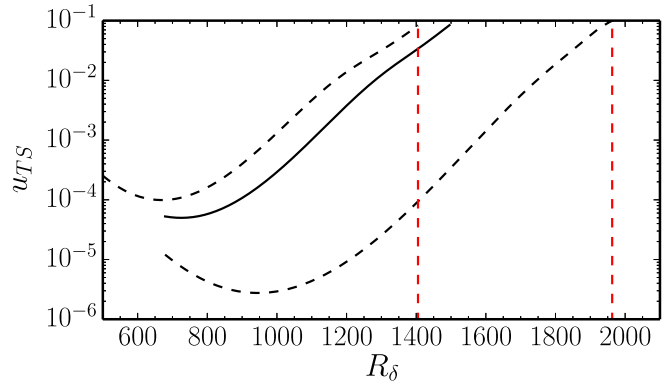

Figure 19. NLPSE simulation of T-S wave growth for $\varepsilon_a = 1\times10^{-3}$, roughness r.m.s. $h^*_{\rm RMS} = 20\mu m$. From right to left in the graph - $n = \{-2, 0, 2\}$. The corresponding frequencies are $F = \{24, 38, 44\}\times10^{-6}$.

VIII. CONCLUSIONS

A numerically efficient and high-fidelity acoustic receptivity method has been described and applied to model the T-S disturbance generation process in the presence of surface roughness. The time-harmonic approach, though computer memory intensive, requires the inversion of a large matrix which is considerably less computationally expensive than time-stepping methods. It is therefore more appropriate for incorporation in advanced optimization tools of laminar flow wing analysis. All of the results reported in this paper were computed on a stan-

dalone multi-core computer. We have demonstrated the basic approach on the Blasius flat plate model, and with continued development the same methodology should be applicable to more practical aerodynamic surfaces.

In incompressible flat plate analysis we have proven that the method provides accurate predictions of receptivity amplitudes both for localized and distributed roughness. The former is presented in the form of the efficiency function, which is geometry-independent, and the non-parallel effects are found to be lower than 10% in the considered range of frequencies and Reynolds numbers. The latter is first compared against local FRNT predictions for two and three-dimensional T-S waves in the presence of wall waviness, providing proof of correctness of our approach and of the numerics. Moreover, when compared with the multiple-scales approach, we confirm its capability to take into account non-parallel effects.

Lastly an uncertainty quantification analysis is undertaken in the presence of two-dimensional distributed random roughness. The mean PSD follows a power law subject to uncertainties following a Gaussian probability distribution. At a constant r.m.s height, the mean PSD of the surface roughness is found to be a key factor in determining the mean receptivity amplitude. This is in accordance with the fundamental view of receptivity as a resonance phenomena - the more energy is contained in the relevant length scales for a given acoustic wave frequency, the higher the amplitude of the resulting T-S disturbance within the boundary layer. The major source of unpredictability in this stochastic process is rooted in the phase differences between the spectral components comprising the roughness field distribution. The effects of any random behavior of the mean PSD over the probability density function of the T-S wave amplitude are minor in comparison. In practical applications the roughness model parameters can be tuned based on measurements of the real surface. Specifically, the roughness r.m.s and the PSD slope k should be determined in order to obtain a realistic model. The amplitudes a_i can also be replaced altogether by an experimentally determined PSD.

The importance of predicting the initial amplitude of boundary layer disturbances has been demonstrated. Realistic transition scenarios can thus be simulated by coupling the variance based receptivity analysis with NLPSE computations to simulate non-linear growth of instabilities, provided characterization of the freestream acoustic and surface roughness fields are available. In our analysis the PSD of the freestream acoustic field is assumed uniform and non-stochastic. A more realistic stochastic-based description (*i.e* based on wind-tunnel measured acoustic PSD, say) is trivial to implement in the overall methodology. The approach provides variance estimates on the most likely transition location; breakdown criteria based on nonlinear PSE simulations are simplistic, nevertheless this analysis was purely for demonstration purposes of how the stochastic nature of the receptivity process feeds through and impacts the latter stages of the laminar-turbulent breakdown. The same analysis could be undertaken with more sophisticated modeling of the latter stages of transition (with full DNS say), using the mean receptivity amplitude and associated variance estimates to stipulate inflow conditions in simulations.

ACKNOWLEDGMENTS

This project has received funding from the European Union's Horizon 2020 research and innovation programme under the Marie Sklodowska-Curie grant agreement No 675008. SM would also like to acknowledge the support from EPSRC grant EP/I037946/1 and the Innovate UK funded ALFET project 113022.

Appendix: Forced Linear Navier-Stokes Equations

Equation (25) can be rewritten as

$$\frac{\partial \hat{u}_c}{\partial x} + \frac{\partial \hat{v}_c}{\partial y} + i\beta\hat{w}_c = 0 \,, \tag{A.1a}$$

$$\begin{aligned}&\frac{1}{R}\left(\frac{\partial^2 \hat{u}_c}{\partial x^2} + \frac{\partial^2 \hat{u}_c}{\partial y^2}\right) - \left(-i\omega + \frac{\beta^2}{R} + \frac{\partial \bar{u}}{\partial x}\right)\hat{u}_c - \frac{\partial \hat{p}_c}{\partial x} \\ &- \bar{v}\frac{\partial \hat{u}_c}{\partial y} - \frac{\partial \bar{u}}{\partial y}\hat{v}_c - \bar{u}\frac{\partial \hat{u}_c}{\partial x} \\ &= u_a\frac{\partial \hat{u}_w}{\partial x} + \hat{u}_w\frac{\partial u_a}{\partial x} + v_a\frac{\partial \hat{u}_w}{\partial y} + \hat{v}_w\frac{\partial u_a}{\partial y} \,,\end{aligned} \tag{A.1b}$$

$$\begin{aligned}&\frac{1}{R}\left(\frac{\partial^2 \hat{v}_c}{\partial x^2} + \frac{\partial^2 \hat{v}_c}{\partial y^2}\right) - \left(-i\omega + \frac{\beta^2}{R} + \frac{\partial \bar{v}}{\partial y}\right)\hat{v}_c - \frac{\partial \hat{p}_c}{\partial y} \\ &- \bar{u}\frac{\partial \hat{v}_c}{\partial x} - \frac{\partial \bar{v}}{\partial x}\hat{u}_c - \bar{v}\frac{\partial \hat{v}_c}{\partial y} \\ &= v_a\frac{\partial \hat{v}_w}{\partial y} + \hat{v}_w\frac{\partial v_a}{\partial y} + u_a\frac{\partial \hat{v}_w}{\partial x} + \hat{u}_w\frac{\partial v_a}{\partial x},\end{aligned} \tag{A.1c}$$

$$\begin{aligned}&\frac{1}{R}\left(\frac{\partial^2 \hat{w}_c}{\partial x^2} + \frac{\partial^2 \hat{w}_c}{\partial y^2}\right) - \left(-i\omega + \frac{\beta^2}{R}\right)\hat{w}_c - i\beta\hat{p}_c \\ &- \bar{v}\frac{\partial \hat{w}_c}{\partial y} - \bar{u}\frac{\partial \hat{w}_c}{\partial x} = v_a\frac{\partial \hat{w}_w}{\partial y} + u_a\frac{\partial \hat{w}_w}{\partial x} \,.\end{aligned} \tag{A.1d}$$

In the above, setting $\omega = 0$, all right-hand side terms to zero, and replacing the subscript c to w, recovers the roughness induced mean-flow distortion Eqs. (23) of §II C.

REFERENCES

[1] W. S. Saric, H. L. Reed, and E. B. White. Stability and transition of three-dimensional boundary layers. Annual Review of Fluid Mechanics, 35(1):413–440, 2003.

[2] P. J. Schmid and D. S. Henningson. Stability and transition in shear flows, volume 142. Springer Science & Business Media, 2012.

[3] L. Brandt. The lift-up effect: the linear mechanism behind transition and turbulence in shear flows. European Journal of Mechanics-B/Fluids, 47:80–96, 2014.

[4]M. V. Morkovin. On the many faces of transition. In C. Sinclair Wells, editor, Viscous Drag Reduction: Proceedings of the Symposium on Viscous Drag Reduction held at the LTV Research Center, Dallas, Texas, September 24 and 25, 1968, pages 1–31, Boston, MA, 1969. Springer US.

[5]J. L. Van Ingen. A suggested semi-empirical method for the calculation of the boundary layer transition region. Technical report, Technische Hogeschool Delft, Vliegtuigbouwkunde, Rapport VTH-74, 1956.

[6]A. M. O. Smith and N. Gamberoni. Transition, pressure gradient and stability theory. Technical report, Douglas Aircraft Co. ES 26388, 1956.

[7]H. Bippes. Basic experiments on transition in three-dimensional boundary layers dominated by crossflow instability. Progress in aerospace sciences, 35(4):363–412, 1999.

[8]D. Arnal. Boundary layer transition: predictions based on linear theory. In AGARD, Special Course on Progress in Transition Modelling 63 p (SEE N94-33884 10-34), 1994.

[9]M. E. Goldstein. The evolution of tollmien–sclichting waves near a leading edge. Journal of Fluid Mechanics, 127:59–81, 1983.

[10]M. E. Goldstein. Scattering of acoustic waves into tollmien-schlichting waves by small streamwise variations in surface geometry. Journal of Fluid Mechanics, 154:509–529, 1985.

[11]A. I. Ruban. On tollmien-schlichting wave generation by sound. In V. V. Kozlov, editor, Laminar-Turbulent Transition, pages 313–320, Berlin, Heidelberg, 1985. Springer Berlin Heidelberg.

[12]S. H. Lam and N. Rott. Theory of linearized time-dependent boundary layers. Technical report, Cornell University GSAE Rep. AFOSR TN–60–1 100, 1960.

[13]K. Stewartson. On the flow near the trailing edge of a flat plate ii. Mathematika, 16(1):106–121, 1969.

[14]K. Stewartson. On laminar boundary layers near corners. Quarterly Journal of Mechanics and Applied Mathematics, 23:137–152, 1970.

[15]A. F. Messiter. Boundary-layer flow near the trailing edge of a flat plate. SIAM Journal on Applied Mathematics, 18(1):241–257, 1970.

[16]R. J. Bodonyi, W. J. C. Welch, P. W. Duck, and M. Tadjfar. A numerical study of the interaction between unsteay free-stream disturbances and localized variations in surface geometry. Journal of Fluid Mechanics, 209:285–308, 1989.

[17]M. Choudhari and C. L. Streett. A finite reynolds-number approach for the prediction of boundary-layer receptivity in localized regions. Physics of Fluids A: Fluid Dynamics, 4(11):2495–2514, 1992.

[18]M. Choudhari. Boundary-layer receptivity due to distributed surface imperfections of a deterministic or random nature. Theoretical and Computational Fluid Dynamics, 4(3):101–117, 1993.

[19]J. D. Crouch. Localized receptivity of boundary layers. Physics of Fluids A: Fluid Dynamics, 4(7):1408–1414, 1992.

[20]J. D. Crouch. Non-localized receptivity of boundary layers. Journal of Fluid Mechanics, 244:567–581, 1992.

[21]J. Crouch and F. P. Bertolotti. Nonlocalized receptivity of boundary layers to three-dimensional disturbances. In 30th Aerospace Sciences Meeting and Exhibit, page 740, 1992.

[22]T. Herbert. Parabolized stability equations. Annual Review of Fluid Mechanics, 29(1):245–283, 1997.

[23]A. H. Nayfeh and O. N. Ashour. Acoustic receptivity of a boundary layer to tollmien–schlichting waves resulting from a finite-height hump at finite reynolds numbers. Physics of Fluids, 6(11):3705–3716, 1994.

[24]W. S. Saric. Physical description of boundary-layer transition: Experimental evidence. In AGARD, Special Course on Progress in Transition Modelling 51 p (SEE N94-33884 10-34), 1994.

[25]X. Wu. Receptivity of boundary layers with distributed roughness to vortical and acoustic disturbances: a second-order asymptotic theory and comparison with experiments. Journal of Fluid Mechanics, 431:91–133, 2001.

[26]M. Wiegel and R. Wlezien. Acoustic receptivity of laminar boundary layers over wavy walls. AIAA Paper, 93–3280, 1993.

[27]F. P. Bertolotti. Receptivity of three-dimensional boundary-layers to localized wall roughness and suction. Physics of Fluids, 12(7):1799–1809, 2000.

[28]M. Bouthier. Stabilité linéaire des écoulements presque parallèles. J. de Mec, 11:599–621, 1972.

[29]M. Gaster. On the effects of boundary-layer growth on flow stability. Journal of Fluid Mechanics, 66(03):465–480, 1974.

[30]W. S. Saric and A. H. Nayfeh. Nonparallel stability of boundary-layer flows. The Physics of Fluids, 18(8):945–950, 1975.

[31]S. Zuccher and P. Luchini. Boundary-layer receptivity to external disturbances using multiple scales. Meccanica, 49(2):441–467, 2014.

[32]F. P. Bertolotti and J. D. Crouch. Simulation of boundary-layer transition: receptivity to spike stage. Technical report, Institute for Computer Applications in Science and Engineerging Hampton VA, 1992.

[33]T. Herbert and N. Lin. Studies of boundary-layer receptivity with parabolized stability equations. AIAA Paper, 93, 1993.

[34]D. C. Hill. Adjoint systems and their role in the receptivity problem for boundary layers. Journal of Fluid Mechanics, 292:183–204, 1995.

[35]C. Airiau. Non-parallel acoustic receptivity of a blasius boundary layer using an adjoint approach. Flow, Turbulence and Combustion, 65(3):347–367, 2000.

[36]S. S. Collis and A. Dobrinsky. Evaluation of adjoint based methods for the prediction of receptivity. In H. F. Fasel and W. S. Saric, editors, Laminar-Turbulent Transition, pages 111–116, Berlin, Heidelberg, 2000. Springer Berlin Heidelberg.

[37]C. Thomas, S. Mughal, and R. Ashworth. On predicting receptivity to surface roughness in a compressible infinite swept wing boundary layer. Physics of Fluids, 29(3):034102, 2017.

[38]J. D. Crouch and P. R. Spalart. A study of non-parallel and nonlinear effects on the localized receptivity of boundary layers. Journal of Fluid Mechanics, 290:29–37, 1995.

[39]Z. Liu, W. Zhao, and C. Liu. Direct numerical simulation of transition in a subsonic airfoil boundary layer. In 35th Aerospace Sciences Meeting and Exhibit, volume 97, page 0752, 1997.

[40]R. S. Lin and H. L. Reed. Navier-stokes simulation of stationary crossflow vortices on a swept wing. Bull. Am. Phys. Soc, 36(10):2631, 1991.

[41]N. De Tullio and A. I. Ruban. A numerical evaluation of the asymptotic theory of receptivity for subsonic compressible boundary layers. Journal of Fluid Mechanics, 771:520–546, 2015.

[42]L. Schrader, L. Brandt, and D. S. Henningson. Receptivity mechanisms in three-dimensional boundary-layer flows. Journal of Fluid Mechanics, 618:209–241, 2009.

[43]N. Shahriari, D. J. Bodony, A. Hanifi, and D. S. Henningson. Acoustic receptivity simulations of flow past a flat plate with elliptic leading edge. Journal of Fluid Mechanics, 800, 2016.

[44]S. S. Collis and S K. Lele. Receptivity to surface roughness near a swept leading edge. Journal of Fluid Mechanics, 380:141168, 1999.

[45]M. H. Carpenter, M. Choudhari, F. Li, C. L. Streett, and C. Chang. Excitation of crossflow instabilities in a swept wing boundary layer. AIAA Paper, 378:2010, 2010.

[46]C. L. Streett. Direct harmonic linear navier-stokes methods for efficient simulation of wave packets. AIAA Paper, 98–0784, 1998.

[47]M. S. Mughal and R. M. Ashworth. Uncertainty quantification based receptivity modelling of crossflow instabilities induced by distributed surface roughness in swept wing boundary layers. In 43rd AIAA Fluid Dynamics Conference, page 3106, 2013.

[48]M. S. Mughal. Advanced transition prediction: Development of linearised navier-stokes receptivity methods. Technical report, Imperial College London, 2012.

[49]H. Schlichting, K. Gersten, E. Krause, H. Oertel, and K. Mayes. Boundary-layer theory, volume 7. Springer, 1960.

[50]P. W. Duck. The response of a laminar boundary layer in supersonic flow to small-amplitude progressive waves. Journal of

Fluid Mechanics, 219:423–448, 1990.

[51] H. B. Keller. A new difference scheme for parabolic problems. In Numerical solutions of partial differential equations, II (Hubbard, B. ed.), pages 327–350. New York: Academic Press, 1971.

[52] M. S. Mughal. Advanced transition prediction - development of linearised navier-stokes receptivity methods, validation and application. Technical report, Imperial College London, 2011.

[53] M. S. Mughal. Copse/bl-mipsecr user manual. Technical report, Imperial College London, 2015.

[54] C. Chang and M. Choudhari. Boundary-layer receptivity and integrated transition prediction. AIAA Paper, 526:2005, 2005.

[55] M. Choudhari and C. Streett. Theoretical prediction of boundary-layer receptivity. In Fluid Dynamics Conference, page 2223, 1994.

[56] R. S. Sayles and T. R. Thomas. Surface topography as a nonstationary random process. Nature, 271(5644):431–434, 1978.

[57] A. Majumdar and C. L. Tien. Fractal characterization and simulation of rough surfaces. Wear, 136(2):313–327, 1990.

[58] B. D. Van Deusen. A statistical technique for the dynamic analysis of vehicles traversing rough yielding and non-yielding surfaces, volume 659. National Aeronautics and Space Administration, 1967.

[59] M. V. Berry and Z. V. Lewis. On the weierstrass-mandelbrot fractal function. Proceedings of the Royal Society of London A: Mathematical, Physical and Engineering Sciences, 370(1743):459–484, 1980.

[60] M. S. Mughal. Active control of wave instabilities in three-dimensional compressible flows. Theoretical and Computational Fluid Dynamics, 12(4):195–217, Dec 1998.

[61] F. P. Bertolotti. Linear and nonlinear stability of boundary layers with streamwise varying properties. Ph.D. thesis, Ohio State University, Columbus, 1991.